Title

- **Long title**: Proteins Derived From MRL/MpJ Tendon Provisional Extracellular Matrix and Secretome Promote Pro-Regenerative Tenocyte Behavior
- **Short title**: MRL Proteins Promote a Pro-Regenerative Phenotype

Authors

Jason C. Marvin,[1] Ethan J. Liu,[2] Hsin Huei Chen,[2] David A. Shiovitz[3], Nelly Andarawis-Puri[2,4]*

Affiliations

[1]Nancy E. and Peter C. Meinig School of Biomedical Engineering, Cornell University, Ithaca, NY 14853, USA

[2]Sibley School of Mechanical and Aerospace Engineering, Cornell University, Cornell University, Ithaca, NY 14853, USA

[3]Phelps Hospital, Tarrytown, NY 10591, USA

[4]Hospital for Special Surgery, New York, NY, USA

*Corresponding author: na424@cornell.edu

Abstract

Tendinopathies are prevalent musculoskeletal conditions that have no effective therapies to attenuate scar formation. In contrast to other adult mammals, the tendons of Murphy Roths Large (MRL/MpJ) mice possess a superior healing capacity following acute and overuse injuries. Here, we hypothesized that the application of biological cues derived from the local MRL/MpJ tendon environment would direct otherwise scar-mediated tenocytes towards a pro-regenerative MRL/MpJ-like phenotype. We identified soluble factors enriched in the secretome of MRL/MpJ tenocytes using bioreactor systems and quantitative proteomics. We then demonstrated that the combined administration of structural and soluble constituents isolated from decellularized MRL/MpJ tendon provisional ECM (dPECM) and the secretome stimulate scar-mediated rodent tenocytes towards enhanced mechanosensitivity, proliferation, intercellular communication, and ECM deposition associated with MRL/MpJ cell behavior. Our findings highlight key biological mechanisms that drive MRL/MpJ tenocyte activity and their interspecies utility to be harnessed for therapeutic strategies that promote pro-regenerative healing outcomes.

Teaser

Proteins enriched in a super-healer mouse strain elicit interspecies utility in promoting pro-regenerative tenocyte behavior.

MAIN TEXT

Introduction

Tendinopathies are debilitating disorders that account for over a third of all musculoskeletal consultations (1). In adult mammals, tendon ruptures heal poorly by forming fibrovascular and mechanically inferior scar tissue ('scar-mediated healing') that

is later remodeled ineffectively by resident tendon cells, or tenocytes. This scar-mediated healing can result in long-term pain, disability, and functional deficits that contribute to a reduced quality of life. Surgical repair remains the gold standard for the clinical treatment of tendon ruptures wherein the torn ends are reattached to restore load transmission and the original tissue functionality. However, these procedures do not address the underlying pathology and suffer from post-operative re-tear rates as high as 94% (2–4). The use of biologic therapies, such as autologous platelet-rich plasma (PRP) injections, to promote tendon healing remains contentious given variable reports of their clinical efficacy in attenuating scar-mediated healing (5,6), which is attributed to a lack of standardization in their manufacturing, quality control, and administration. Clearly, understanding the biological mechanisms underpinning tendon regeneration is critical to development of more effective therapeutics.

The Murphy Roths Large (MRL/MpJ) mouse strain harbors a natural regenerative capacity in several tissues and organs (7,8), including tendon (9–15). We have previously shown that MRL/MpJ tendons exhibit vastly improved structural and mechanical recovery as compared to canonical healing C57BL/6 (B6) tendons following acute laceration/full-thickness hole punch or overuse injuries (9,12,13), thereby establishing the promise of the MRL/MpJ mouse strain for expanding our mechanistic understanding of scarless tendon healing. Using *ex vivo* organ culture to eliminate any systemic contributions to healing, we previously found that hole-punched MRL/MpJ tendons showed significantly increased bulk mechanical properties compared to those of B6 tendons at 4 weeks post-injury (wpi). These findings suggest that the local tendon environment consisting of resident tenocytes and the extracellular matrix (ECM), primarily drive MRL/MpJ scarless tendon healing (11,12), which raised the question of whether the MRL/MpJ tendon ECM can ameliorate otherwise scar-mediated healing outcomes. Subsequent *in vivo* assessment of the therapeutic utility of a PEG-4MAL hydrogel incorporated with decellularized MRL/MpJ tendon provisional ECM (dPECM), a temporary bioactive ECM produced during the proliferative phase of healing, improved B6 tendon alignment, cell elongation, and stiffness compared to untreated tendons by 6 weeks post-implantation (16). Moreover, in that study, we identified a subset of proteins that are uniquely enriched in the MRL/MpJ tendon dPECM that may contribute to these improved healing outcomes. However, native tissue mechanical properties were not fully recovered despite the enhanced structure achieved using these dPECM constructs. While decellularization of tissue samples for dPECM collection is necessary to prevent immunogenicity, this technique removes resident tenocytes and most of their direct contributions within the tendon. These findings suggest that supplementation of tenocyte-secreted soluble factors, otherwise known as the secretome, may augment the therapeutic potency of the MRL/MpJ tendon dPECM.

This study aims to (*i*) **comparatively characterize B6 and MRL/MpJ tenocyte behavior to establish robust cellular metrics that delineate scar-mediated and scarless tendon healing**, (*ii*) identify soluble factors enriched in the MRL/MpJ tenocyte secretome, and (*iii*) determine whether the administration of MRL/MpJ-enriched soluble and ECM proteins together is functionally advantageous in stimulating pro-regenerative MRL/MpJ-like activity compared to either constituent alone. We addressed these goals by adopting an experimental approach integrating primary cell culture, functional *in vitro* assays, and *in vivo* histological analyses that capture physiological aspects of acute tendon healing and quantitative proteomics to profile the secretome. We hypothesized that harnessing biological cues derived from the local MRL/MpJ tendon environment through recombinant protein design would recapitulate the beneficial effects of administering these

MRL/MpJ constituents *in vitro.* Our findings shed insight into the cellular processes and candidate protein regulators that drive effective mammalian tendon healing across rodent species, establishing a novel biologics-based therapeutic strategy that also provides a promising platform for future mechanistic interrogation.

Results

MRL/MpJ tenocytes demonstrate greater intercellular communication, cytoskeletal organization, mechanosensitivity, and ECM deposition than B6 tenocytes

We have previously shown that culturing B6 tenocytes on MRL/MpJ dPECM-coated 2D substrates attained a dendritic morphology consisting of axon-like protrusions and decreased circularity(12). To ascertain whether these protrusions are reflective of MRL/MpJ tenocyte behavior, we analyzed the single-cell morphology of B6 and MRL/MpJ tenocytes cultured on collagen I-coated substrates using phalloidin staining (**Fig. 1A and B**). Compared with B6 tenocytes, a significantly greater proportion of MRL/MpJ tenocytes formed actin-rich protrusions (70.3% compared to 88.9% of all cells, $P = 0.034$; **Fig. 1C**). There were no differences in the number of protrusions formed on a per cell basis between B6 and MRL/MpJ tenocytes (data not shown), indicating that the significantly greater total protrusion length (total and normalized to cell spreading area; $P < 0.0001$ and 0.0029, respectively) observed in MRL/MpJ tenocytes (**Fig. 1C**) is due to longer cytoskeletal extensions. Importantly, these results confirm that our prior observations are characteristic of MRL/MpJ tenocyte morphology that may mediate long-distance cell-cell contacts and could be suggestive of increased mechanosensitivity. Additionally, MRL/MpJ tenocytes also showed significantly lower cell circularity ($P = 0.0001$) and greater spreading area ($P = 0.03$) and perimeter ($P < 0.0001$) (**Fig. 1D**), which corroborates our prior morphological observations in B6 tenocytes cultured on MRL/MpJ dPECM also as characteristic of MRL/MpJ cell behavior. We next investigated whether these intrinsic differences in the actin cytoskeleton serve as a physical mediator to enable MRL/MpJ tenocytes to better engage with changes to their surrounding microenvironment.

It is well established that the contractile actomyosin machinery is required to drive changes in cell shape, adhesion, and motility that regulate cell signaling and behavior (17). In particular, actin-based cellular protrusions facilitate cell migration and spreading and are closely coupled with the formation of focal adhesions (FAs) such as vinculin. Vinculin regulates the recruitment and disassembly of these FAs that link the actin cytoskeleton to the ECM and enable cells to sense and respond to environmental factors (e.g., activation of growth factor-mediated signaling pathways, mechanical cues) (18–21). Thus, we hypothesized that the protrusion networks that are characteristic of MRL/MpJ tenocytes enhance mechanosensitivity and cell migration. Indeed, MRL/MpJ tenocytes exhibited significantly greater FA number (1.77-fold higher, $P < 0.0001$) and area (1.6-fold higher, $P = 0.0012$) than that of B6 tenocytes when cultured on collagen I-coated substrates (**Fig. 1E**). However, when normalized to cell spreading area, FA area was not statistically different between B6 and MRL/MpJ cells (data not shown; $P = 0.22$), but FA number remained significantly higher in MRL/MpJ tenocytes ($P = 0.001$). Moreover, the average FA size was significantly greater in B6 tenocytes than MRL/MpJ tenocytes (1.16 ± 0.064 μm^2 compared to 0.96 ± 0.05 μm^2), indicating that these MRL/MpJ protrusions are stabilized by smaller nascent adhesions(20) (<1 μm diameter). These findings indicate that MRL/MpJ tenocytes undergo rapid and robust turnover of smaller FAs that better stabilize the actin cytoskeleton and its integrin-mediated mechanotransduction compared to B6

148 tenocytes. Furthermore, 2D wound scratch assays (**Fig. 1F**) showed significantly increased
149 MRL/MpJ tenocyte numbers at the defect site compared to B6 tenocytes on fibronectin-
150 coated substrates ($P = 0.048$; **Fig. 1G**). Cell migration was not different on collagen I-
151 coated substrates ($P = 0.25$) despite comparable protrusion networks on both collagen I
152 and fibronectin (**Fig. 1H**), indicating that changes to other cell-ECM and/or cell-cell
153 interactions during an injury response likely play a more important role in modulating 2D
154 tenocyte migration.
155
156 Cytoskeletal tension-induced activation of Hippo pathway effectors and transcriptional
157 coactivators, Yes-associated protein (YAP) and WW domain-containing transcription
158 regulator protein 1 (TAZ), regulates cell mechanosensing and adhesion-mediated
159 signaling (22–25). To ascertain whether our observations of increased stress fiber, FA, and
160 cellular protrusion formation in MRL/MpJ tenocytes is indicative of a YAP-dependent
161 mechanosignaling program, we next evaluated the effects of inhibiting actin stabilization
162 and ROCK-mediated cell contractility on YAP nuclear translocation. We cultured B6 and
163 MRL/MpJ tenocytes at low density on collagen I-coated substrates with and without
164 Latrunculin A (inhibitor of actin polymerization), blebbistatin (inhibitor of myosin II, a
165 downstream effector of ROCK), and Y-27632 (inhibitor of ROCK) for 4 hours and stained
166 for YAP (**Fig. 1I**). As expected, YAP nuclear translocation was significantly greater in
167 MRL/MpJ tenocytes than B6 tenocytes (1.46-fold higher, $P < 0.0001$) treated with the
168 DMSO vehicle control (**Fig. 1J**). No correlations were found between YAP nuclear
169 translocation and single-cell morphological parameters. To account for baseline
170 differences in YAP nuclear translocation between B6 and MRL/MpJ tenocytes, we
171 subsequently normalized data relative to the DMSO control and compared the relative
172 changes in YAP nuclear translocation with pharmacological inhibition between mouse
173 strains (**Fig. 1K**). Unsurprisingly, disruption of the actin cytoskeleton with Latrunculin A
174 treatment resulted in YAP being predominantly localized in the cytoplasm with no
175 difference in relative YAP nuclear translocation between B6 and MRL/MpJ tenocytes (P
176 $= 0.22$), indicating that actin polymerization is required for nuclear transport of YAP.
177 Inhibition of myosin II with blebbistatin treatment significantly reduced relative YAP
178 nuclear translocation in MRL/MpJ tenocytes compared to B6 tenocytes ($P < 0.0001$) with
179 MRL/MpJ tenocytes having greater cytoplasmic retention of YAP. Similarly, inhibition of
180 ROCK with Y-27632 treatment reduced relative YAP nuclear translocation in MRL/MpJ
181 tenocytes compared to B6 tenocytes ($P = 0.058$). These data confirm that MRL/MpJ
182 tenocytes harbor enhanced mechanosignaling dependent on myosin II- and ROCK-
183 mediated contractility to facilitate YAP nuclear translocation.
184
185 We next extended our characterization of B6 and MRL/MpJ cell behavior to confluent
186 culture conditions that are more reflective of the dPECM environment during the
187 proliferative phase of acute tendon healing at 7 dpi *in vivo* (11). After 7 days of culture in
188 full-serum media to reach confluency (**Fig. 2A**), cytoskeletal and cell-deposited
189 fibronectin coherency/alignment (**Fig. 2B-D**) were significantly greater in MRL/MpJ
190 tenocytes than B6 tenocytes (both $P < 0.0001$), consistent with early improvements in
191 cellular and ECM organization seen at 7 dpi *in vivo* in MRL/MpJ tendons compared to B6
192 tendons (11). Remarkably, many MRL/MpJ nuclei also assembled into tightly-packed,
193 linear arrays along fibronectin tracks (yellow dashed line; **Fig. 2C**) that closely resembled
194 physiological tendon organization despite the absence of structural or mechanical cues
195 during culture. MRL/MpJ tenocytes also exhibited significantly greater ECM deposition
196 (1.46- and 1.29-fold higher for fibronectin and collagen I, respectively; $P < 0.0001$ for
197 both) and thickness ($P = 0.0021$ for fibronectin), cell number (1.50-fold higher, $P <$

198 0.0001), and expression of connexin-43 (Cx-43) gap junctions ($P = 0.0089$) compared to
199 B6 tenocytes (**Fig. 2E and F**). Moreover, the increasingly anisotropic and fibrillar
200 fibronectin network generated by MRL/MpJ tenocytes is consistent with ROCK- and
201 mechanosignaling-mediated (e.g., ITGB1, FAK) pathways being known to regulate
202 fibronectin assembly (26–29). Visually, fibronectin and Cx-43 gap junctions were more
203 uniformly distributed throughout neighboring MRL/MpJ tenocytes, whereas these were
204 limited to the periphery of B6 tenocytes suggestive of disrupted cell-ECM adhesion
205 (yellow arrowheads, **Fig. 2C**). However, it is not clear whether increased Cx-43 gap
206 junction formation is characteristic of MRL/MpJ tenocyte behavior or driven by changes
207 in cell density. To overcome this limitation, we next cultured cells for 3 days in full-serum
208 media to yield comparable densities. Cx-43 expression remained significantly higher in
209 MRL/MpJ tenocytes than B6 cells (1.32-fold higher, $P = 0.024$) and predominantly
210 localized at the tips of actin-based cellular protrusions at cell-cell contact sites (yellow
211 arrowheads, **Fig. 2G**). There were no differences in αSMA expression after 3 ($P = 0.6$)
212 and 7 (2.2% lower, $P = 0.14$) days of culture (**Fig. 2H**), indicating that increased
213 cytoskeletal organization of MRL/MpJ tenocytes at confluency is not primarily mediated
214 by myofibroblast activity. In short, our data demonstrate that enhanced cytoskeletal and
215 ECM alignment, ECM deposition, and intercellular communication are fundamental to
216 MRL/MpJ tenocyte behavior and likely contribute to improved structural healing
217 outcomes.
218
219 After elucidating key biological processes underlying MRL/MpJ tenocyte behavior, we
220 next focused on another central question of this study. Can we harness MRL/MpJ tendon
221 ECM- and cell-derived factors to effectively reprogram otherwise scar-mediated B6
222 tenocytes toward a pro-regenerative MRL/MpJ-like phenotype? To answer this question,
223 we first used quantitative proteomics to identify growth factors and cytokines enriched in
224 the MRL/MpJ tenocyte secretome. We next interrogated the biochemical milieu of the
225 local MRL/MpJ tendon environment by culturing B6 and MRL/MpJ tenocytes using a
226 combination of their dPECM-coated substrates (12) and the secretome.
227
228 **The MRL/MpJ tenocyte secretome contains distinct biological signatures to those of**
229 **B6 tenocytes regardless of loading modality**
230 We first comprehensively characterized soluble proteins in B6 and MRL/MpJ tenocyte
231 secretomes by profiling concentrated static and dynamic (i.e., cells conditioned under
232 cyclic stretch using the CellScale MCFX bioreactor system) conditioned media samples
233 for up to 640 and 200 protein targets, respectively, using Quantibody Mouse Cytokine
234 Arrays (**Fig. 3A**). Due to sample volume constraints using the MCFX bioreactor compared
235 to traditional culture flasks, quantitative proteomics of the dynamic secretome was
236 restricted to 200 targets. There were no differences in protein concentration (**Fig. S1A**) or
237 cell number at the time of conditioned media collection (data not shown) between B6 and
238 MRL/MpJ secretome samples. In the static secretome (**Fig. 3B**), we identified 336
239 cytokines of which 252 (75% of detected proteins) were differentially expressed proteins
240 (DEPs) between B6 (50.9% of detected proteins, 118 enriched in B6, 53 only detected in
241 B6) and MRL/MpJ tenocytes (24.1% of detected proteins, 74 enriched in MRL/MpJ, 7
242 only detected in MRL/MpJ). In the dynamic secretome (**Fig. 3B**), we identified 56
243 cytokines of which 43 (76.8% of detected proteins) were differentially expressed between
244 B6 (44.6% of detected proteins, 21 enriched in B6, 4 only detected in B6) and MRL/MpJ
245 tenocytes (32.1% of detected proteins, 17 enriched in MRL/MpJ, and 1 only detected in
246 MRL/MpJ). Of note, interleukin-3 (IL-3) was only detected in the B6 secretomes, tumor
247 necrosis factor alpha (TNF-α) was only detected in the dynamic secretomes, and TNF

248 receptor 2 (TNF RII), thymic stromal lymphopoietin (TLSP), and nephrilysin were only
249 detected in the static secretomes. We applied multivariate analyses using principal
250 components analysis (PCA; **Fig. 3C**) and found that B6 and MRL/MpJ static secretomes
251 formed separate clusters along PC1 (34.4% of total variance). PCA revealed minor
252 overlap of B6 and MRL/MpJ dynamic secretome samples reflective of higher biological
253 variation. Heatmap visualization corroborated these observations as evidenced by a greater
254 degree of sample clustering in the static secretomes (**Fig. 3D**) compared to the dynamic
255 secretomes (**Fig. 3E**). We performed Kyoto Encyclopedia of Genes and Genomes
256 (KEGG) overrepresentation analysis of all static secretome DEPs using a dot plot and
257 implicated several inflammatory pathways, including tumor necrosis factor (TNF), toll-
258 like receptor (TLR), nuclear factor-kappa B (NF-κB), T and B cell receptor, interleukin,
259 cytokine, and chemokine signaling (**Fig. S2A**). Supporting our YAP data in the present
260 study, our IPA upstream regulator analysis found that Rho-associated protein kinase 1
261 (ROCK1) and other putative drivers of YAP activation (integrin beta-1; ITGB1, focal
262 adhesion kinase; FAK, Ras-related C3 botulinum toxin substrate 1; Rac1) were predicted
263 to be upregulated in the MRL/MpJ static secretome.
264
265 On the basis that tenocytes experience cyclic stretching due to dynamic tensile loading, we
266 next conducted comparative analyses of the static and dynamic secretomes using IPA to
267 determine canonical pathways, upstream regulators, and diseases and functions that are
268 differentially regulated with mechanical stimulation. Surprisingly, mechanical stimulation
269 had a minimal effect on the majority of diseases and functions (**Fig. 3F and Table S2**) and
270 canonical pathways (**Fig. 3G**)—most of which are involved in inflammation and cell
271 death—with similar Z-score activation patterns between the static and dynamic
272 secretomes. In contrast, minimal agreement was found for upstream regulators with 8 of
273 the top 10 annotations having contrasting activation states (**Fig. S1B**), suggesting
274 molecular changes in B6 and MRL/MpJ tenocyte activity with mechanical stimulation that
275 nonetheless lead to comparable cellular functions and outcomes. To assess the effects of
276 mechanical stimulation on the secretion of soluble factors detected in both secretome
277 datasets, we next compared the relative change in protein concentrations for 46 cytokines
278 shared between the static and dynamic secretomes. Interestingly, we found that B6 and
279 MRL/MpJ dynamic secretomes showed similar fold change expression for 37 cytokines
280 (80.4% of total) compared to their respective static secretomes (**Fig. 3H**). Overall, these
281 distinct paracrine signaling signatures between B6 and MRL/MpJ tenocytes regardless of
282 loading modality illustrate further cell-intrinsic differences that distinguish scar-mediated
283 and scarless tendon healing outcomes.
284
285 **Adult quiescent MRL/MpJ tenocytes undergo greater proliferative and apoptotic**
286 **activity compared to B6 tenocytes**
287 Altered cell cycle control (e.g., elevated G2/M accumulation) has been proposed as a
288 potential characteristic of the regenerative MRL/MpJ cell phenotype (7), leading us to
289 next characterize the growth kinetics and endogenous β-Galactosidase (β-Gal) activity, a
290 marker for cellular senescence (i.e., irreversible cell cycle arrest), between B6 and
291 MRL/MpJ tenocytes (**Fig. 4A and B**). B6 tenocytes showed a significantly higher
292 percentage of β-Gal-positive/senescent cells at passage four (45.4%, $P = 0.022$) and five
293 (60.7%, $P < 0.0001$) compared to passage three (25.3%; **Fig 4C**). In contrast, MRL/MpJ
294 tenocytes displayed minimal cellular senescence with no significant changes in β-Gal
295 expression with increasing passage numbers (0.3%, 1%, and 6%; **Fig. 4C**). These results
296 were accompanied by a progressive decline in B6 tenocyte population doubling time
297 (PDT) with serially passaging, whereas MRL/MpJ tenocyte PDT remained constant and

was significantly lower than that of B6 cells at passage four (1.99-fold lower, $P = 0.032$) (**Fig. 4D**). Although growth rates were comparable at earlier passages, cumulative population doubling (CPD) at passage four was significantly greater in MRL/MpJ tenocytes compared to B6 tenocytes (1.32-fold higher, $P = 0.0048$). At each passage, both the percentage ($P = 0.003$ at P3, < 0.0001 at P4, < 0.0001 at P5) and number of senescent cells ($P = 0.018$ at P3, < 0.0001 at P4, < 0.0001 and P5; **Fig. S3A**) were significantly higher in B6 tenocytes compared to MRL tenocytes. The total cell number was not different between B6 and MRL/MpJ tenocytes (**Fig. S3B**). Collectively, these data demonstrate that MRL/MpJ tenocytes are more resistant to replicative senescence and exhibit superior expansion potential compared to B6 tenocytes. Given that growth arrest and resistance to pro-apoptotic stimuli are hallmarks of cellular senescence (30,31), we next performed immunohistochemical (IHC) analysis of Ki-67 and cleaved caspase-3, markers of cell proliferation and apoptosis respectively, of injured B6 and MRL/MpJ patellar tendons during the proliferative and remodeling phases of healing (**Fig. 4E**). As expected, MRL/MpJ tendons had significantly increased cell proliferation (**Fig. 4F**) and apoptosis (**Fig. 4G**) compared to B6 tendons at 1 wpi (Ki-67: $P < 0.0001$, caspase-3: $P = 0.0032$) and 4 wpi (Ki-67: $P = 0.0027$, caspase-3: $P = 0.029$), providing evidence that corroborates the relevance of our *in vitro* findings as potentially conserved mechanisms at play during the more complex *in vivo* healing environment.

The p53/p21 signaling axis is thought to play a critical role in MRL/MpJ tissue regeneration wherein the absence of p21 promotes senescence, hyperproliferation, and the DNA damage response (32). Notably, $p21^{-/-}$ knockout and MRL/MpJ mice are capable of regenerating full-thickness ear and articular cartilage defects (32,33). To determine whether reduced p21 expression and endogenous DNA damage are associated with MRL/MpJ tenocyte behavior *in vitro*, we stained B6 and MRL/MpJ cells for endogenous p21 and γH2AX. Contrary to reports of linking appendage regeneration to a lack of p21 expression in MRL/MpJ ear fibroblasts(32), we detected endogenous p21 activity in MRL/MpJ tenocytes (**Fig. 4H**). There were no differences in the number of γH2AX-positive foci that mark DNA double-stranded breaks (**Fig. S4A**) or p21 expression (**Fig. S4B**), indicating that MRL/MpJ tenocyte quiescence and proliferation may be regulated independently of p21 and DNA damage repair mechanisms.

To investigate the biological processes underlying MRL/MpJ tenocyte behavior, we next investigated cell-intrinsic differences in morphology and function associated with homeostasis and wound healing.

B6 and MRL/MpJ tenocytes treated with MRL/MpJ-derived proteins attain comparable single-cell morphology and cell-ECM interactions

We have previously shown that dPECM harvested from MRL/MpJ tendon at 1 wpi enhance B6 tenocyte cell morphology and proliferation *in vitro*. Additionally, comparative analyses results in IPA showed similar biological annotations between the static and dynamic secretomes, motivating the use of the static secretome in subsequent experiments for practicality. Accordingly, we investigated three experimental conditions: (*i*) a scar-mediated healing group of B6 tenocytes treated with B6-derived components (i.e., dPECM and secretome) (referred to as 'BB'), (*ii*) a therapeutic group of B6 tenocytes treated with MRL/MpJ-derived components (referred to as 'BM'), and (*iii*) a positive control group of MRL/MpJ tenocytes treated with MRL/MpJ-derived components (referred to as 'MM').

347 Strikingly, B6 and MRL/MpJ tenocytes at a low cell density treated with MRL/MpJ-
348 derived components displayed identical single-cell morphology, FA formation, and
349 cellular protrusion patterns (**Fig. 5A and B**). In contrast, BB exhibited significantly higher
350 cell circularity and lower perimeter, number of FAs and total FA area, and protrusion
351 parameters (percentage of cells with protrusions, number of protrusions, total protrusion
352 length, total protrusion length normalized to cell perimeter) compared to BM and MM
353 (**Fig. 5D-F**). Additionally, B6 tenocytes treated with MRL/MpJ-derived components
354 exhibited significantly higher αSMA expression compared to B6 tenocytes treated with
355 B6-derived components ($P = 0.016$) or at baseline ($P < 0.0001$) (**Fig. 5G and H**),
356 suggesting that myofibroblast activity is transiently increased but does not remain elevated
357 with extended culture periods. Interestingly, B6-derived components elicited little or no
358 effect with BB being largely comparable to untreated B6 tenocytes. Supporting our
359 hypothesis, these findings demonstrate that MRL/MpJ-derived components reprogram cell
360 morphology and amplify mechanotransduction pathways towards MRL/MpJ tenocyte
361 behavior.
362
363 We next assessed the capacity of MRL/MpJ-derived components to enhance cytoskeletal
364 organization, ECM deposition, and Cx-43 formation in confluent B6 tenocytes (**Fig. 6A**).
365 To minimize the influence of serum proteins and confounding effects from differences in
366 total cell number due to increased MRL/MpJ tenocyte proliferation, cells were seeded at a
367 high density and subsequently maintained in low-serum media with or without exogenous
368 secretome supplementation. Moreover, to definitively ascertain whether there is a
369 combined benefit of administering the MRL/MpJ-derived components, we also cultured
370 B6 tenocytes with MRL/MpJ dPECM or secretome alone with cells cultured in only low-
371 serum media served as baseline controls. Consistent with our previous baseline B6 and
372 MRL/MpJ comparisons under culture in full-serum media, MRL/MpJ tenocytes showed
373 greater baseline F-actin alignment ($P = 0.0003$), fibronectin deposition (1.20-fold higher,
374 $P = 0.095$), collagen I deposition (1.15-fold higher, $P = 0.0029$), and no difference in
375 αSMA expression compared to B6 tenocytes (**Fig. 6B**). In contrast with our previous data
376 in full-serum media, MRL/MpJ tenocytes exhibited significantly lower baseline Cx-43
377 expression than B6 tenocytes under low-serum conditions (1.96-fold lower, $P < 0.0001$).
378 Supporting our hypothesis, B6 and MRL/MpJ tenocytes treated with MRL/MpJ-derived
379 components showed comparable F-actin alignment and relative changes in fibronectin
380 deposition that were significantly higher than that of B6 tenocytes treated with B6-derived
381 components (**Fig. 6C and D**). BM also showed greater collagen I deposition compared to
382 BB ($P = 0.10$) (**Fig. S6A**). Due to restricted ECM deposition under low-serum conditions,
383 fibronectin alignment could not be quantified. Contrary to our hypothesis, BB and BM had
384 comparable Cx-43 expression that were significantly lower than MM. However, these
385 discrepancies are largely attributed to a nearly two-fold reduction in Cx-43 expression in
386 MRL/MpJ at baseline, as evidenced by comparable staining profiles between cells that
387 received any combination of mouse-derived components. This data suggest that these
388 tenocytes upregulate Cx-43 expression in response to mitogenic stimulation. There were
389 no differences in αSMA expression between all treatment groups. Further supporting our
390 hypothesis, F-actin alignment and Cx-43 levels were significantly higher in B6 tenocytes
391 treated with MRL/MpJ-derived components compared to dPECM ($P = 0.0031$ for F-actin
392 and $P < 0.0001$ for Cx-43) or secretome ($P = 0.031$ for F-actin and $P = 0.002$ for Cx-43)
393 alone (**Fig. 6E**), confirming the combined benefit of administering the MRL/MpJ-derived
394 components.
395

Lastly, we determined whether MRL/MpJ-derived components could promote cell proliferation and attenuate the onset of cellular senescence by treating B6 tenocytes cultured at a moderate density for 3 days and staining for ß-gal activity (**Fig. 6F**). There was no difference in cell number between B6 and MRL/MpJ tenocytes at baseline or between cells treated with MRL/MpJ-derived components. Supporting our hypothesis, compared with BB, BM showed significantly increased total cell number (1.17-fold higher, $P = 0.045$). In addition, total cell number was significantly higher in B6 tenocytes treated with MRL/MpJ-derived components compared to dPECM ($P = 0.036$) or secretome ($P = 0.0002$) alone (**Fig. 6G**). These results are consistent with previous observations that an early increase in tenocyte proliferation is a hallmark of MRL/MpJ tendon healing(10,12). However, contrary to our hypothesis, there was no difference in the number or percentage of senescent cells between BB and BM. B6 tenocytes treated with only secretome exhibited less senescence overall compared to BM (1.15-fold lower, $P = 0.074$), but no differences were found in the number of senescent cells between all B6 tenocyte groups. Altogether, these findings demonstrate that MRL/MpJ-derived components potently augment B6 tenocytes towards pro-regenerative MRL/MpJ-like behavior despite the persistence of a senescent subpopulation of cells.

Collectively, our data provide compelling evidence that the combined administration of MRL/MpJ-derived components modulates B6 tenocytes toward an MRL/MpJ-like cell phenotype. However, there are important considerations in harnessing these biological cues for therapeutic delivery. First, the tendon ECM and secretome each contain thousands of biomolecules (34,35), which can preclude their feasibility to scale up for preclinical testing in animal models. Second, it remains unclear whether these hallmarks of MRL/MpJ tenocyte behavior and the therapeutic utility of MRL/MpJ-derived components are conserved across other mammalian species. To address these points, we sought to develop a panel of recombinant proteins using our quantitative proteomics datasets. The final objective of this study was to assess the functional activity of B6-derived components, MRL/MpJ-derived components, and the recombinant protein therapeutic *in vitro* on patellar tenocytes derived from scar-mediated healing Sprague-Dawley (SD) rats. We hypothesized that the recombinant protein therapeutic will recapitulate the effects of the MRL/MpJ-derived components on rat tenocyte behavior *in vitro* and that these changes will be consistent with our mouse data.

Recombinant protein therapeutic promotes regenerative MRL/MpJ-like tenocyte behavior across species

Mouse and rat models closely recapitulate human tendon anatomy and physiology (36,37), supporting the use of rodent tenocytes to investigate the proof-of-concept translational capacity of our recombinant protein therapeutic. However, despite the prevalent use of rodent models for tendon research, a comparative evaluation of baseline mouse and rat tenocytes behavior is lacking. Accordingly, we first cultured B6 and SD patellar tenocytes on collagen I-coated substrates and analyzed their single-cell morphology. There were no differences in any morphological (cell circularity, spreading area, perimeter), cellular protrusion parameters (percentage of cells with protrusions, number of protrusions, total protrusion length), or αSMA expression between B6 and SD tenocytes (**Fig. S7A and B**)

A candidate panel of 29 recombinant proteins (10 structural and 19 soluble, 12 of which were from the secretome) was identified from a systemic screen of our quantitative proteomics data (**Table 1**). However, a preliminary set of 17 recombinant proteins (indicated in bold) were employed in the present study for our protein therapeutic (**Fig.**

446 **7A**) due to several proteins being on backorder or lacking commercial availability at the
447 time of investigation. To mimic our combined dPECM and secretome culture system with
448 the recombinant protein therapeutic, structural proteins were sequentially adhered onto a
449 collagen I-coated substrate starting with acid-solubilized proteins followed by those
450 reconstituted in sterile 1X PBS. Soluble proteins were supplemented into low-serum
451 media. All protein concentrations used in this study were determined from published
452 reference values for *in vitro* administration. We then investigated three experimental
453 conditions: (*i*) a scar-mediated healing group of SD tenocytes treated with B6-derived
454 components (referred to as 'RB'), (*ii*) a positive control group of SD tenocytes treated
455 with MRL/MpJ-derived components (referred to as 'RM'), and (*iii*) the therapeutic group
456 of SD tenocytes treated with the recombinant protein therapeutic (referred to as 'RP'). For
457 the B6-derived components, B6 uninjured dECM was used as the substrate coating instead
458 of the dPECM to match the conditions analyzed via mass spectrometry in our published *in*
459 *vivo* study (16).
460
461 Based on our results that cell morphology is preserved across B6 and SD tenocytes, we
462 were able to definitively ascertain the effects of our recombinant protein therapeutic on
463 SD tenocyte behavior. Compared with MRL/MpJ-derived components, the recombinant
464 protein therapeutic increased the number of protrusions ($P = 0.0088$) and total protrusion
465 length ($P = 0.09$, 0.041 when normalized to cell perimeter) (**Fig. 7B and C**). Additionally,
466 there were no differences in the number of protrusions or total protrusion coverage
467 (normalized to cell perimeter) between RB, RM, or baseline. As expected, SD tenocytes
468 cultured with the recombinant protein therapeutic and MRL/MpJ-derived components
469 exhibited comparable cell circularity, spreading area, and αSMA expression (**Fig. 7D**).
470 Supporting our hypotheses, RM and RP exhibited significantly lower circularity and
471 higher perimeter, spreading area, αSMA expression, percentage of cells with protrusions,
472 and total protrusion length compared to RB. Taken together, these results establish that the
473 morphological features of MRL/MpJ tenocyte can be achieved in SD tenocytes through
474 the selective delivery of key proteins. Further supporting our hypotheses, SD tenocytes
475 treated with the recombinant protein therapeutic and MRL/MpJ-derived components
476 showed comparable F-actin alignment and were significantly higher than that of SD
477 tenocytes treated with B6-derived components ($P < 0.0001$ for both) (**Fig. 7E and F**).
478 Moreover, RP displayed significantly higher F-actin alignment compared to RM ($P =$
479 0.02). Contrary to our hypothesis, while the recombinant protein therapeutic ($P = 0.09$)
480 and MRL/MpJ components ($P = 0.37$) increased fibronectin deposition compared to the
481 baseline control, these changes were not statistically significant. However, this may
482 potentially be attributed to the recombinant protein therapeutic only containing 17 out of
483 the 29 identified candidates. Lastly, we found significantly lower total cell number in RP
484 compared to RM (9.8% lower; $P = 0.04$), suggesting that the recombinant protein
485 therapeutic induces apoptosis that leads to more effective cytoskeletal alignment
486 consistent with increased cell turnover during MRL/MpJ scarless tendon healing *in vivo*.
487
488
489 **Discussion**
490
491 The widespread benefits of using tissue-specific dECM (38,39) and mesenchymal
492 stem/progenitor cell-sourced secretome (35,40) to stimulate tissue repair and regeneration
493 have been thoroughly established. However, there has been little exploration on the effects
494 of these components together despite their capability to support complex cell-ECM and
495 cell-cell interactions. Supporting the use of this combined biologic approach, our study

integrated the structural constituents and cell-secreted soluble factors enriched in the MRL/MpJ tendon dPECM and secretome to modulate scar-mediated healing tenocytes towards an MRL/MpJ-like phenotype *in vitro*. These findings also provide mechanistic insight into the biological processes underlying regenerative MRL/MpJ tenocyte behavior and establish *in vitro* metrics grounded in physiologically relevant *in vivo* acute injury outcome measures. A major hurdle to harnessing the MRL/MpJ dPECM and secretome for therapeutic applications is that they each contain thousands of biomolecules, most of which may not be essential in delineating scar-mediated and regenerative healing, which presents challenges in translating these components for larger animal testing. Accordingly, our study isolated a panel of candidate protein regulators of mammalian tendon regeneration that exerts interspecies utility by enhancing scar-mediated healing rat tenocyte activity. Our data showed that rat tenocytes treated with the recombinant protein therapeutic outperformed the MRL/MpJ-derived components as evidenced by increased cellular protrusion formation and cytoskeletal alignment. These findings indicate that our approach of selectively administering recombinant proteins is functionally advantageous, which may be attributed to limiting unnecessary protein-protein interactions and instead achieving more targeted modulation of the molecular processes and downstream effectors that regulate MRL/MpJ cell behavior.

Constitutive stabilization of HIF-1α expression and p21 downregulation have both also been shown to control ear wound regeneration in adult MRL/MpJ mice (7,41). In contrast, multilineage differentiation, pluripotency markers, and HIF-1α expression were not observed in this study. We also found no difference in p21 expression between B6 and MRL/MpJ tenocytes consistent with findings reported by Lalley *et al* (10). Therefore, our data implicate resident tenocyte or progenitor cell populations as key mediators of MRL/MpJ tendon healing outcomes. Supporting our proposed paradigm, Grinstein *et al*. (42) recently identified a latent population of *Axin2*$^{+}$ tenocytes in the midsubstance of mouse and human tendons that is recruited to the injury site, proliferate, and transiently adopt injury responsive states to centrally organize the healing response. Our results illustrated that rodent tenocytes treated with MRL/MpJ-derived components or our recombinant protein therapeutic are robustly reprogrammed *in vitro* to attain morphological characteristics identical to those of MRL/MpJ tenocytes. This observation generates an exciting direction for future studies to determine whether adult scar-mediated healing tenocytes retain a pro-regenerative capacity that is activated upon exposure to therapeutic interventions *in vivo*.

Although healthy tenocytes were collected from young adult animals in this study, a quarter of B6 tenocytes expressed senescent ß-gal activity whereas MRL/MpJ tenocytes maintained a minimally senescent phenotype. Some studies have causally related TSDC and tenocyte senescence to pathological aging and chronic degenerative tendinopathy, whereby their accumulation leads to diminished tenogenic differentiation and cytoskeletal organization, reduced cell migration, upregulation of proinflammatory signaling cascades, and aberrant ECM remodeling (43–46). These changes extended to B6 tenocytes in our data when comparatively evaluating baseline B6 and MRL/MpJ tenocyte behavior *in vitro*. Similarly, Kallenbach and Freeberg *et al*. recently reported downregulated senescence-associated pathways in MRL/MpJ flexor tendon healing compared to that of B6 using bulk transcriptomic analyses (14). However, to our surprise and contrary to our ß-gal staining data, the static secretome of MRL/MpJ tenocytes was enriched for more known human senescence-associated secretory phenotype (SASP) factors (47) compared to that of B6 tenocytes, suggesting a potentially beneficial and tissue-dependent context

546 for some of these SASP factors. Mounting evidence has shown that other regenerative
547 animal models such as zebrafish and amphibians undergo tissue damage-induced cellular
548 senescence that is localized to the injury site (48,49). Additionally, genetic or
549 pharmacological (e.g., senolytic and senomorphic agents) removal of senescent cells *in*
550 *vivo* has resulted in both reparative and impaired healing outcomes (49–51), underscoring
551 divergent roles of developmentally- and injury-induced cellular senescence during wound
552 healing. Considering that MRL/MpJ-derived components shifted B6 tenocytes towards a
553 pro-regenerative phenotype without affecting the number of senescent cells, we speculate
554 that these MRL/MpJ-enriched proteins overcome the degenerative ECM response
555 associated with senescence and maintain some degree of phenotypic reprogramming even
556 on senescent cells, as evidenced by consistent changes to their single-cell morphology.
557 Future work should determine the extent to which these senescent tenocytes react to
558 treatment by examining single-cell parameters in ß-gal-positive tenocytes via multiplexed
559 IF staining.
560
561 Our findings establish that the enhanced cell contractility that defines the MRL/MpJ
562 tenocyte phenotype are stabilized by the formation of cellular protrusions and focal
563 adhesions. Scar-mediated rodent tenocytes treated with MRL/MpJ-derived components or
564 our recombinant protein therapeutic not only mimicked these cellular features but also
565 activated a more contractile myofibroblastic phenotype. Relatedly, Alisafaei *et al*. (52)
566 recently discovered a positive two-way feedback loop between cellular protrusion
567 dynamics and local ECM and mechanical anisotropy that promote fibroblastic activation
568 and effective collagen remodeling. Moreover, we and others (53) have shown that
569 connexin-43 localizes along tenocyte processes before assembling into cell-cell gap
570 junctions at higher cell densities. Connexin-43 is the most abundant gap junction present
571 in adult tendons, forming longitudinal and lateral contacts that regulate cellular
572 metabolism, mechanosensitivity (e.g., stretch-induced calcium and ATP release), and
573 intercellular communication through paracrine and autocrine effects (54–56). Taken
574 together, these results suggest that early upregulation of connexin-43 activity through
575 mitogenic stimulation with MRL/MpJ-derived components or the recombinant protein
576 therapeutic facilitates an expedited healing response characterized by increased tenocyte
577 proliferation, migration, and fibronectin deposition. Fibronectin is key constituent of the
578 provisional ECM that guides cell adhesion, collagen assembly and fibrillogenesis, and
579 temporal sequestration and release of soluble factors to further modulate cell behavior
580 (57,58). Aberrant fibronectin accumulation is associated with long-term myofibroblast
581 survival and persistence that ultimately drives scar-mediated tendon healing (59–61). In
582 the context of the proliferative phase of acute tendon healing, our *in vitro* data suggest that
583 MRL/MpJ tenocytes rapidly proliferate and undergo transient increases in αSMA
584 expression and cell contractility, which self-regulates their cytoskeletal organization to
585 enable early deposition of highly aligned fibronectin networks that promote cell migration
586 and remodeling activity. Supporting these proposed cellular mechanisms, cell proliferation
587 and apoptosis remained significantly elevated in MRL/MpJ tendons compared to B6
588 tendons at 1 and 4 wpi following acute injury *in vivo* in the present study. This data
589 indicates a high turnover capacity of the MRL/MpJ tendon environment in actively
590 recruiting cells throughout the proliferative and remodeling phases of healing to resolve
591 the injury site while simultaneously preventing excessive ECM deposition that leads to
592 scar formation. Overall, these findings shed light into the biological mechanisms that can
593 inform the development of therapeutics for mammalian tendon regeneration.
594

595 This study is not without some limitations. First, the tendon sheath was excluded when
596 isolating primary tendon cells as established by Bi *et al* (62). As this study also did not
597 assess the presence of TSPCs *in vivo*, the precise functional contributions of sheath-
598 derived TSPCs in MRL/MpJ tendon regeneration remain to be elucidated. Second,
599 Quantibody-based proteomics are limited to preselected cytokine targets, are unable to
600 distinguish between latent and active forms (e.g., matrix metalloproteinases; MMPs), and
601 typically cannot recognize pro-peptides and membrane-bound cytokines (e.g., activin,
602 IGF, TGFß). Despite these concerns, Quantibody assays offer pg-level sensitivity greater
603 than that of traditional liquid chromatography-mass spectrometry (LC-MS) techniques
604 (63) and thus allow for the quantitative detection of rare and low-abundance soluble
605 proteins that are capable of engaging in ligand-receptor signaling. However, LC-MS
606 technologies remain the analytical standard for deciphering a wide range of large intact
607 proteins that comprise the ECM composition. Third, our study only analyzed male animals
608 for generating primary cell lines, dPECM, and secretome as well as functional assays. We
609 have recently shown that adult male and female MRL/MpJ tendons both demonstrate a
610 regenerative capacity with vastly improved mechanical recovery compared to those of B6
611 mice (13). More recently, we also found that both male and female MRL/MpJ tenocytes
612 exhibit similar or superior *in vitro* outcome measures, as detailed in the present study,
613 compared to B6 tenocytes (64). These findings suggest that the cellular and molecular
614 mechanisms underlying MRL/MpJ tendon regeneration are largely conserved between
615 sexes. Future experiments should further investigate the extent of sexual dimorphism in
616 MRL/MpJ tendon regeneration and ensure that the recombinant protein therapeutic
617 similarly modulates female rodent tenocytes towards an MRL/MpJ-like phenotype.
618
619 There are several technical and scientific considerations in moving towards *in vivo*
620 delivery of this recombinant protein therapeutic into clinically relevant tendon injuries in
621 larger animal models. First, the present study only evaluated a subset of 17 out of the 29
622 proteins identified from the quantitative proteomic analyses of the tendon ECM and
623 secretome. We anticipate that the incorporation of the remaining 12 proteins will amplify
624 the observed therapeutic effects on scar-mediated tenocytes (e.g., ECM deposition). The
625 integration of these proteins and their different molecular weights, isoelectric points, and
626 half-life properties is non-trivial from a drug delivery perspective. Furthermore, as not all
627 29 recombinant proteins may be necessary to achieve therapeutic efficacy *in vivo,* other
628 ongoing efforts will further refine this panel and assess its efficacy in tendon healing in
629 both acute and chronic overuse injuries. Recent studies have demonstrated that functional
630 blockade of molecular targets elevated during scar-mediated healing using neutralizing
631 antibodies *in vivo* ameliorated overuse-induced tendinopathy in mice (65). While our
632 study focused on evaluating the factors enriched in the MRL/MpJ tendon biological
633 environment, it should be noted that more than half of all cytokines in the static secretome
634 were increased or exclusively secreted by B6 tenocytes. Future studies will interrogate
635 whether the inhibition of B6-enriched soluble factors can further augment the therapeutic
636 potential of our MRL/MpJ-informed protein therapeutic.
637
638 We have previously demonstrated that MRL/MpJ tendons retain their improved healing
639 capacity compared to B6 tendons when isolated from the systemic environment during *ex*
640 *vivo* organ culture (12). In addition, we and other groups have shown reduced macrophage
641 infiltration (10) and attenuated inflammatory pathways (11,13,14) in MRL/MpJ tendons
642 compared to B6 tendons during the proliferative phase of healing. These observations
643 motivated our overarching hypothesis that the local tissue environment is the primary
644 driver of MRL/MpJ tendon regeneration. Interestingly, the top four soluble proteins

645 enriched in the MRL/MpJ static secretome that were evaluated in this study – CXCL5
646 (LIX), CXCL1 (KC), macrophage inflammatory protein 2 (MIP-2), and semamorphin-3F
647 (SEMA3F) – are chemokines and cytokines known to be potent mediators of early
648 neutrophil recruitment and retainment (66–70). In contrast, decreased circulating serum
649 levels of LIX, KC, MIP-2α during acute tendon injury have been attributed to the
650 regeneration of MRL/MpJ ear wounds (68) and tendons (14). Therefore, we postulate that
651 altered crosstalk between tenocytes and tissue-resident immune cells (e.g., macrophages)
652 or locally directed molecular cues may prompt neutrophils to initiate MRL/MpJ tendon
653 healing by concurrently streamlining the clearance of damaged tissue and the production
654 of the provisional ECM. Nonetheless, future studies should resolve the temporal
655 progression of the inflammatory cascade in MRL/MpJ tendon regeneration and assess the
656 potential immunomodulatory effects of the recombinant protein therapeutic *in vivo*.
657 Lastly, our study identified dual-specificity phosphatase 1 (DUSP1) as the most activated
658 upstream regulator in the B6 static secretome. DUSP1 is capable of dephosphorylating
659 major cell signaling pathways involved in innate immunity, cellular metabolism, and ECM
660 remodeling, including extracellular-signal regulated kinase (ERK) 1/2, mitogen-activated
661 protein kinase (MAPK), and c-Jun N-terminal kinase (JNK) (71–73). Conversely,
662 upstream analysis of the MRL/MpJ static secretome revealed activation of ERK, p38
663 MAPK, and Jun, thus suggesting that these pathways may be upregulated in MRL/MpJ
664 tendon regeneration and could be the basis for future mechanistic interrogation.
665
666 In summary, we demonstrate that the biological mechanisms underlying MRL/MpJ
667 tenocyte behavior can be induced across different mammalian species using a subset of
668 recombinant proteins, which may ultimately have transformative impact for promoting
669 tendon regeneration.
670

671 **Materials and Methods**

672 **Experimental Design**

673 The objective of this study was to assess the utility of MRL/MpJ tendon ECM- and
674 secretome-derived proteins in promoting regenerative outcomes across different species of
675 tenocytes. First, we identified cellular and biological processes that delineate scar-
676 mediated B6 and regenerative MRL/MpJ tenocyte behavior using primary cell culture
677 assays and confocal microscopy. Next, we demonstrated that the combined administration
678 of secretome and decellularized provisional ECM (dPECM) obtained from healthy
679 MRL/MpJ cells and hole-punched tendons at 7 dpi, respectively, modulates B6 cells
680 toward an MRL/MpJ-like phenotype *in vitro*. Lastly, we identified key constituents
681 enriched in the MRL/MpJ secretome using quantitative proteomics and subsequently
682 evaluated the functional activity of a panel of structural and soluble recombinant proteins
683 on rat tenocytes *in vitro*. We hypothesized that selectively delivering this panel of
684 recombinant proteins will recapitulate the effects of the MRL/MpJ-derived components on
685 tenocyte behavior. We further hypothesized that this therapeutic will elicit interspecies
686 utility as a novel therapeutic strategy for tendon healing. All experiments were carried out
687 at passage three (mouse) or passage four (rat) with a minimum of three biological
688 replicates (*N*) unless specified otherwise. For each biological replicate, three technical
689 replicates (*n*) were included.
690

691 **Animals and patellar tendon midsubstance punch injury**

692 All animal procedures were approved by the Cornell University Institutional Animal Care
693 and Use Committee (IACUC). Male 16- to 18-week-old B6 and MRL/MpJ mice were
694 bred in-house with the original dame and sire purchased from The Jackson Laboratory (B6

695 #000664 and MRL/MpJ #000486), unless specified otherwise, with five animals housed
696 per cage. Male 9- to 10-month-old SD rats were purchased from Envigo (#002) with two
697 animals housed per cage. Animals were maintained under alternating 12-hour light/dark
698 cycles with ad libitum access to food and water.
699
700 To generate tendon dPECM, a full-thickness midsubstance injury was introduced into the
701 left patellar tendon of male B6 and MRL/MpJ mice as described previously(12). Briefly,
702 mice were anesthetized with isoflurane (2% volume, 0.3 L/min) and received an
703 intraperitoneal administration of buprenorphine (1 mg/kg body weight). The fur was then
704 completely removed from the left leg before exposing the patellar tendon through a skin
705 incision above the knee cavity. A custom-machined stainless-steel backing (1.5-mm
706 width, 0.5-mm thickness) coated with a polyurethane adhesive (#1867T2; McMaster-Carr)
707 was inserted beneath the tendon before excising the tissue using a 1-mm biopsy punch.
708 After the backing was removed, the skin incision was closed using 6-0 Prolene sutures
709 (#8695G; Ethicon Inc.). Mice resumed cage activity and were euthanized after 1 wpi by
710 CO_2 administration followed by cervical dislocation. The provisional and contralateral
711 tendons were immediately harvested, snap-frozen in liquid nitrogen, and stored at -80°C
712 until use.
713
714 **Primary cell culture and reagents**
715 Low-glucose Dulbecco's modified Eagle's medium (#10-014; Corning) and lot-selected
716 fetal bovine serum (FBS; #35-015-CV; Corning) were used for primary cell expansion and
717 all experiments. Mouse cells were harvested from the patellar tendons of B6 and
718 MRL/MpJ mice as described previously(12). The tendon sheath and fat pad were removed
719 before enzymatic digestion with a mixture of collagenase type I (2 mg/mL) and
720 collagenase type IV (1 mg/mL) in serum-free media for up to 2 hours at 37°C on a rocking
721 shaker. To isolate primary tenocytes, tissue digests were passed through a 70-µm strainer.
722 Rat cells were similarly harvested from the patellar tendons of SD rats as described above
723 except the sheath remained intact. Independent cell isolation batches consisted of patellar
724 tendons pooled from five mice or one rat and served as biological replicates.
725
726 Cells were cultured in DMEM supplemented with 10% FBS and 1% antibiotics-
727 antimycotics (penicillin-streptomycin-amphotericin B; PSA; Gibco) (full-serum media) at
728 37°C and 5% CO_2 with media replenished every 2 days. Cells were routinely passaged at
729 80-90% confluency. For 2D ECM substrates, rat tail collagen I (#A1048301; Thermo
730 Fisher Scientific) and human plasma fibronectin (#33-016-015; Thermo Fisher Scientific)
731 were used. All cell lines employed in this study tested negative for mycoplasma
732 contamination (#LT07-703; Lonza).
733
734 **Immunofluorescence staining and confocal microscopy of cultured tenocytes**
735 For all immunofluorescence experiments, cells were cultured in glass-bottom 96-well
736 plates (#655892; Greiner Bio-One). Antibody details are available in the Supplementary
737 Materials (**Table S1**). Cells were fixed with 2% paraformaldehyde (PFA) for 10 minutes,
738 4% PFA for 20 minutes, washed thrice with 1X PBS, permeabilized with 0.1% Triton X-
739 100 for 15 minutes, and blocked with 3% bovine serum albumin (BSA; in 1X PBS) for 1
740 hour. Primary antibodies (in 3% BSA) were incubated overnight at 4°C unless specified
741 otherwise. Cells were then washed thrice with 1X PBS before incubating with secondary
742 antibodies (in 3% BSA) for 1 hour at room temperature in the dark. Lastly, cells were
743 washed thrice with 1X PBS, counterstained with DAPI (1:1000 dilution in 1X PBS;
744 #D1306; Thermo Fisher Scientific) for 30 minutes, and finally rinsed twice with 1X PBS

745 before imaging. For ECM staining, primary antibodies for fibronectin and collagen I were
746 incubated prior to permeabilization as to only label cell-deposited ECM.
747
748 Images were acquired using a Zeiss LSM710 confocal microscope (Zeiss) using a 25X
749 magnification water-immersion objective. Identical acquisition parameters were used
750 across samples for each independent experiment. All image analyses were conducted in
751 ImageJ (National Institutes of Health) by a blinded user.
752
753 **Tendon decellularization and preparation of dPECM coatings**
754 Tendons harvested from B6 and MRL mice were decellularized using a detergent-free
755 protocol inside a biosafety cabinet (BSC) as described previously (12,74). Briefly, the
756 tissues were incubated with 50 nM of Latrunculin B (#2182-1; BioVision) in DMEM for 2
757 hours at 37°C at 450 RPM to depolymerize actin networks. All subsequent incubation
758 steps were supplemented with 1X protease inhibitor cocktail (#78425; Thermo Fisher
759 Scientific) and conducted at room temperature at 450 RPM to minimize proteolysis. The
760 tissues were washed with deionized water for 30 minutes after Latrunculin B and
761 hypertonic incubation steps. After exposure to Latrunculin B, the tissues were incubated in
762 0.6 M KCl for 2 hours, 1.0 M KI for 2 hours, and then washed in DI water for 12 hours
763 followed by repeated KCl and KI incubation steps to induce osmolysis. Lastly, the tissues
764 were subsequently incubated in 1X phosphate-buffered saline (PBS) containing 1 kU/mL
765 of Pierce™ Universal Nuclease (#88702; Thermo Fisher Scientific) for 2 hours followed
766 by two consecutive 24-hour 1X PBS wash steps to clear residual cellular debris.
767 Decellularized tissues were lyophilized for 72 hours before being snap-frozen,
768 mechanically homogenized (Bread Ruptor 24, Omni, Inc.) using 2.8-mm ceramic beads
769 (#19-646; Omni, Inc.), solubilized (10 mg dry weight/mL) in 1 mg/mL pepsin (#P7012; in
770 0.1 M HCl; Sigma-Aldrich) for 72 hours at 4°C at 150 RPM, and stored at -80°C until use.
771 Flat-bottom 96-well plates were coated with solubilized dPECM (1 mg dry weight/mL
772 diluted in 0.1 M AcOH) overnight at 4°C. Coatings were washed twice with 1X PBS
773 immediately before use to remove residual acid.
774
775 To assess the contributions of the MRL/MpJ-derived components in modulating B6 cells
776 toward an MRL/MpJ-like phenotype, the following experimental groups were evaluated
777 for single-cell morphology and confluent mouse cell experiments: (1) B6 or MRL/MpJ
778 cells alone, (2) cells cultured with only dPECM, (3) cells cultured with only secretome,
779 and (4) cells cultured with both dPECM and secretome. MRL/MpJ cells treated with
780 MRL/MpJ-derived components served as a positive control.
781
782 **Secretome preparation and quantitative proteomics**
783 To generate the static secretome, B6 and MRL/MpJ cells were seeded at 90% confluency
784 on Nunc™ EasYFlask™ culture flasks (#159910; Thermo Fisher Scientific), rinsed once
785 with 1X DPBS (#21-030-CV; Corning), and subsequently incubated with phenol red-free,
786 serum-free media (#11054020, Thermo Fisher Scientific) supplemented with 2X
787 GlutaMAX™ (#35050061; Thermo Fisher Scientific) for 24 hours. The conditioned
788 medium was then collected, concentrated using ultrafiltration centrifugal devices (#88526;
789 3 kDa molecular weight cutoff; polyethersulfone membrane; Thermo Fisher Scientific),
790 and stored at -80°C until use.
791
792 To investigate the effect of mechanical stimulation on the secretome composition, silicone
793 well plates designed for the CellScale MCFX bioreactor (CellScale Biomaterials Testing)
794 were functionalized by surface silanization as described previously (75,76). Briefly,

795 silicone plates were plasma treated for 5 minutes followed by incubation with 10% (3-
796 aminopropyl)triethoxysilane (APTES; #440140; Sigma-Aldrich) in ethanol at 60°C for 60
797 minutes. The plates were then washed thrice with 1X PBS (#21-040; Corning), incubated
798 with 3% glutaraldehyde (#16539-60; Electron Microscopy Sciences) for 20 minutes at
799 room temperature, and rinsed twice with 1X DPBS before covalently coating the
800 substrates with provisional B6 and MRL/MpJ dPECM (1 mg/mL) overnight at 4°C. B6
801 and MRL/MpJ cells were seeded onto their respective dPECM-coated plates in full-serum
802 media and allowed to adhere for 12 hours to reach 90% confluency. To generate the
803 dynamic secretome, cells were then rinsed once with 1X PBS, incubated with serum-free
804 media supplemented with 2X GlutaMAX™, and immediately subjected to a homeostatic
805 uniaxial cyclic stretch regimen (4% sinusoidal strain at 1 Hz; additional details available
806 in Supplementary Materials) for 24 hours before collecting and concentrating the
807 conditioned medium as described above. Streptomycin is known to block stretch-activated
808 ion channels (77), so cells used for dynamic secretome collection were cultured in
809 medium without PSA.
810
811 Secretome was diluted to a 2X final working concentration for all *in vitro* experiments,
812 which was determined as the optimal concentration for promoting B6 tenocyte
813 proliferation (data not shown), in DMEM supplemented with 1% FBS and 1% PSA (low-
814 serum media) to limit the effect of high-abundance serum proteins. Secretome-containing
815 media was replenished every two days from the same batch to ensure consistency between
816 biological replicates. For quantitative proteomics ($N = 3$ per group), conditioned media
817 was normalized to total protein concentration as determined using the bicinchoninic acid
818 (BCA) assay (#23225; Thermo Fisher Scientific) and outsourced to RayBiotech to analyze
819 the cytokine concentrations of the static (Quantibody® Mouse Cytokine Array Q640; up to
820 640 targets) and dynamic secretomes (Quantibody® Mouse Cytokine Array Q4000; up to
821 200 targets). Secretome samples were processed and analyzed in the same batch for each
822 loading condition to minimize variation.
823
824 **Secretome proteomics bioinformatic analyses and visualization**
825 Any detected cytokines that were not within 75% of the lower limit of detection (LOD) of
826 the array were omitted from subsequent analyses. Cytokines with at least two uniquely
827 detected samples that were ≥ 1.2-fold change or only detected in one genotype were
828 regarded as differentially expressed proteins (DEPs). No comparisons for cytokines shared
829 between the static and dynamic secretomes were conducted as these conditions were
830 analyzed using different array technologies. Hierarchical cluster analysis was performed
831 using the online ClustVis (78) web tool to generate heatmap expression patterns of Z-
832 score normalized protein data for the static and dynamic secretomes. Differences between
833 secretome conditions were visualized by clustering biological replicates using
834 unsupervised principal components analysis (PCA). Canonical pathways, upstream
835 regulators, and disease and functions ($P \leq 0.05$ and | Z-score | ≥ 1.5) were performed using
836 Ingenuity Pathway Analysis (IPA; Qiagen). Positive and negative Z-score values indicate
837 predicted activation and inhibition, respectively, of biological functions determined by
838 IPA. For comparative analyses in IPA, a fold change of 2.0 was assigned as a placeholder
839 value to cytokines that were only detected in one genotype. Functional annotation of
840 KEGG pathway enrichment analyses and GO terms were performed in R and DAVID,
841 respectively.
842
843 **Immunohistochemical analysis of cell proliferation and apoptosis in B6 and**
844 **MRL/MpJ acute tendon injuries**

845 Male 12- to 13-week-old B6 and MRL/MpJ mice were purchased from The Jackson
846 Laboratory and underwent a 0.75-mm full-thickness midsubstance injury. Mice were
847 euthanized after 1 and 4 wpi to harvest the provisional tendons. Contralateral patellar
848 tendons harvested at 24-hours post-injury from a separate study were used as naïve
849 uninjured controls. Tendons were fixed in zinc formalin (#5701ZF, Thermo Fisher
850 Scientific), embedded in paraffin, and sectioned coronally at a thickness of 6 µm. All
851 subsequent immunohistochemical staining and image analysis were performed at the
852 midsubstance injury site by a blinded user. To measure cell proliferation and apoptosis,
853 sections were stained for cleaved caspase 3 and Ki-67, counterstained with toluidine blue,
854 and then imaged and stitched (Zeiss AxioVision; Oberkochen, Germany) at 20X
855 magnification. The number of positive and total cells were counted at the injury site in
856 ImageJ to calculate the percentage of apoptotic cells (*N* = 6-9 per group). Sections were
857 also stained for fibronectin using a custom MATLAB code to quantify the percentage of
858 positively-stained matrix (*N* = 6-9 per group) taken at 5X magnification.
859
860 **Cell senescence and population growth assays**
861 To evaluate the effect of serial passaging on cell growth, B6 and MRL/MpJ cells were
862 continuously cultured from P2-P4 (*N* = 5 per group averaged from n = 3 technical
863 replicates per *N*) and counted using a hemocytometer to calculate population doubling
864 level (PDL; **Equation 1**) and population doubling time (PDT; **Equation 2**):
865

$$PDL = PDL_0 + 3.322(\log \frac{N_f}{N_i}) \quad (1)$$

866

$$PDT = T * \frac{\log(2)}{\log(\frac{Nf}{N0})} \quad (2)$$

867
868 Where N_f is the cell number at the time of passage, N_i is the initial cell number seeded into
869 the flask, PDL_0 is the population doubling level of the previous passage, and T is the
870 culture period in hours. B6 and MRL/MpJ cells were then seeded at P3-P5 (5,000
871 cells/well) onto uncoated substrates in full-serum media and allowed to adhere for 24
872 hours. Cells were stained for β-galactosidase (β-Gal) as a marker of senescence using a
873 commercial kit (#9860S; Cell Signaling Technology) and imaged under an inverted
874 brightfield microscope at 10X magnification. The percentage of senescent cells (*N* = 5 per
875 group averaged from n = 3 technical replicates per *N*) was quantified at P3-P5 by counting
876 the number β-gal-positive and total cells. Static secretome DEPs were mapped onto a
877 published human SASP proteomic atlas(47) to correlate cellular senescence to biological
878 function.
879
880 To investigate the role of the dPECM and secretome in regulating cell senescence and
881 proliferation, B6 and MRL/MpJ cells were seeded (5,000 cells/well) onto uncoated or
882 dPECM-coated substrates in full-serum media and allowed to adhere for 24 hours. Cells
883 were then cultured in either low-serum or secretome-containing media for 3 days and
884 analyzed for β-Gal staining (*N* = 5 per group averaged from n = 3 technical replicates per
885 *N*) as described above.
886
887 **Immunofluorescence staining for p21 and DNA damage**
888 To measure p21 activity and intrinsic DNA damage, B6 and MRL/MpJ tenocytes were
889 seeded in full-serum media at a moderate density (5,000 cells/well) on uncoated substrates
890 and allowed to adhere for 24 hours. Cells were then washed once with 1X DPBS and

subsequently cultured in low-serum media for 24 hours prior to staining for p21 and γH2AX. The nuclear p21 integrated density was averaged for all cells in each representative image ($N = 3$ and $n = 24$ images per group). For γH2AX, the number of positive foci ($N = 3$ and $n = 215$-216 cells per group) and pan-nuclear integrated density were measured. ($N = 3$ and $n = 24$ images per group).

Pharmacological inhibition of cytoskeletal tension and organization

B6 and MRL/MpJ cells were seeded (750 cells/well) onto collagen I-coated (50 µg/mL) substrates in full-serum media and allowed to adhere for 24 hours. To modulate cytoskeletal tension, cells were treated for 4 hours with inhibitors against myosin II (blebbistatin at 50 µM in DMSO; #B0560; Sigma-Aldrich), ROCK (Y-27632 at 50 µM in DMSO; #1254; Tocris Bioscience), and actin polymerization (Latrunculin A at 0.5 µM in DMSO; #10010630; Cayman Chemical Company). Cells treated with 0.1% DMSO served as controls.

To assess differences in B6 and MRL/MpJ cell mechanotransduction and morphology, cells were stained for the YAP and F-actin. YAP nuclear localization (nuclear-to-cytoplasmic mean intensity ratio) and single-cell morphology (circularity; **Equation 3**, perimeter, area, and F-actin integrated density) were thresholded and quantified ($n = 72$ cells per group, 8 cells per well).

$$Circularity = 4\pi * \frac{Area}{Perimeter^2} \tag{3}$$

Cell migration assay

For 2D cell migration experiments ($N = 5$ per group averaged from n = 3 technical replicates per N), 96-well plates were coated overnight at 4°C with collagen I (50 µg/mL; #A1048301; Thermo Fischer Scientific) or fibronectin (50 µg/mL; #33-016-015; Thermo Fisher Scientific) to recapitulate biochemical cues associated with homeostasis and wound healing, respectively. B6 and MRL/MpJ cells were seeded (7,500 cells/well) onto collagen I- and fibronectin-coated substrates in full-serum media and allowed to adhere for 12 hours. Cells were serum starved in low-serum media for 18 hours to induce cell cycle synchronization, manually scratched using a 200 µL pipette tip, rinsed once with 1X DPBS, and subsequently cultured in low-serum media.

Transmitted light images were taken using a SpectraMax i3x Multi-Mode Microplate Reader (Molecular Devices). The number of cells that migrated into the defect region was quantified for 0- and 12-hours post-wounding.

Modulating single-cell morphology, cytoskeletal protrusions, and focal adhesions

To assess whether MRL/MpJ components are capable of shifting B6 cell morphology toward previous observations(12) of decreased cell circularity and enhanced cytoskeletal protrusions, B6 and MRL/MpJ cells were seeded (750 cells/well) onto collagen I- or dPECM-coated substrates in full-serum media and allowed to adhere for 18 hours. Cells were serum starved in low-serum media for 24 hours and cultured in either low-serum or secretome-containing media for 24 hours. To assess differences in cell morphology and focal adhesion formation, cells were stained for F-actin and vinculin, respectively.

Single-cell morphology was thresholded and quantified. Cytoskeletal protrusion metrics (total number of protrusions, maximum protrusion length, total protrusion length) were

939 manually measured using the freehand line tool for all protrusions greater than 25 μm in
940 length. Semi-automated quantification of focal adhesions (total number of focal adhesions,
941 average focal adhesion area, number of focal adhesions normalized to cell area) was
942 performed as described previously (79). All experiments were analyzed with $N = 3$ per
943 group and up to $n = 54$ cells per group with an equal number of cells randomly selected
944 from each well.
945
946 **Stimulating cytoskeletal alignment, matrix deposition, and gap junction formation**
947 B6 and MRL/MpJ cells were seeded (2,000 cells/well) onto uncoated substrates and
948 cultured in full-serum media for 3 or 7 days. Media was changed every 2 days. To compare
949 baseline behavior for cytoskeletal alignment, matrix deposition, intercellular
950 communication, and myofibroblast activity, cells were stained for F-actin, fibronectin,
951 collagen I, Cx-43 gap junctions, and αSMA, respectively. Cytoskeletal alignment was
952 calculated as the local coherency/alignment index of F-actin stress fibers averaged over five
953 elliptical regions of interest (ROIs) for each representative image using the OrientationJ
954 (80) plugin. A coherency value of 1 indicates high anisotropy with perfectly aligned fibers,
955 whereas a value close to 0 indicates high isotropy with no preferential fiber alignment. Cx-
956 43 levels were measured as the integrated density normalized to cell number. Fibronectin
957 fibril alignment was similarly analyzed as described above. Fibronectin and collagen I
958 deposition were measured by normalizing the integrated density to the cell number of each
959 representative image. Myofibroblast activity was measured total αSMA integrated density.
960 Fibronectin and collagen I thickness were measured as the maximum intensity projection of
961 Z-stack images ($N = 3$ and $n = 27$ Z-stacks per group). All other outcome measures were
962 analyzed with $N = 3$ per group and up to $n = 45$ images per group with an equal number of
963 images randomly taken in each well.
964
965 To assess whether MRL/MpJ components are capable of shifting confluent B6 cells
966 toward an MRL/MpJ-like phenotype, B6 and MRL/MpJ cells were seeded (7,500
967 cells/well) onto uncoated or dPECM-coated substrates in full-serum media and allowed to
968 adhere for 24 hours. Cells were then cultured in either low-serum or secretome-media for
969 7 days. Media was changed every 2 days. Cytoskeletal alignment, matrix deposition,
970 intercellular communication, and myofibroblast activity were assessed by staining and
971 analyzing cells for F-actin, fibronectin, Cx-43, and αSMA. Cells were also stained for
972 collagen I deposition by measuring the integrated density normalized to cell number.
973 Fibronectin fibril alignment could not be analyzed due to insufficient ECM deposition
974 under low-serum culture conditions. All outcome measures were analyzed with $N = 3$ per
975 group and up to $n = 45$ images per group with an equal number of images randomly taken
976 in each well.
977
978 **Development of recombinant protein therapeutic and functional activity on rat cells**
979 Proteomic analyses of the mouse patellar tendon (MRL/MpJ 1-week dPECM compared to
980 B6 uninjured dECM) and secretome identified proteins of interest (POIs) for in vitro
981 investigation. Structural POIs with at least two unique peptides and that were ≥ 2-fold
982 higher in the MRL/MpJ 1-week dPECM ($P \leq 0.1$) were collectively applied onto collagen
983 I-coated substrates. Soluble POIs with at least two detected samples and that were ≥ 1.2-
984 fold higher ($P \leq 0.05$) were supplemented in low-serum media. A candidate panel of 29
985 POIs (10 structural and 19 soluble) were identified, 17 of which were evaluated as a
986 preliminary subset in this study (**Table 1**). All POIs were prepared fresh from the same
987 batch of stock solution to minimize the impact of freeze-thawing on protein stability.
988 Structural POIs were administered by first applying acid soluble proteins (in 0.1 M

AcOH) onto an existing base collagen I coating (50 µg/mL) overnight at 4°C. After washing twice with 1X PBS to remove residual acid, non-acid soluble POIs were then applied (in 1X PBS) overnight at 4°C. After washing twice again with 1X PBS, SD tenocytes were seeded (750 cells/well) onto POI-coated substrates in full-serum media and allowed to adhere for 18-24 hours.

To assess whether the recombinant protein therapeutic elicits a similar effect as MRL-derived components across different species of tenocytes, the following experimental groups were evaluated for single-cell morphology and confluent cell experiments: (1) rat cells alone, (2) cells cultured with dPECM (B6 uninjured or MRL/MpJ 1-week provisional) and secretome (B6 or MRL/MpJ), and (3) cells cultured with the POIs. For single-cell experiments, adhered SD tenocytes were serum starved in low-serum media for 24 hours and cultured in either low-serum or soluble POI-containing media for 24 hours. For confluent cell experiments, adhered SD tenocytes were cultured in either low-serum or soluble POI-containing media for 7 days. Media was changed every 2 days.

Rat single-cell morphology, cytoskeletal protrusion metrics, and aSMA integrated density were analyzed as described above ($N = 3$ and $n = 72$ cells per group). Cytoskeletal alignment and fibronectin deposition were analyzed as described above ($N = 3$ and $n = 45$ images per group).

Statistical Analysis

Baseline comparisons between B6 and MRL/MpJ cells or B6 and rat cells were performed using a Welch's *t*-test for single-cell morphology and confluent cell parameters, a Mann-Whitney *U* test for integrated density data, a Kolmogorov–Smirnov test for number of cytoskeletal protrusions, or a Student's *t*-test for all other outcome measures. Comparisons between treatment groups were performed using a one-way Welch ANOVA with Games-Howell's multiple comparisons test for single-cell morphology and confluent cell parameters, or a Kruskal-Wallis test with Dunn's multiple comparisons test for integrated density data. Cell senescence and population growth kinetics were compared between mouse genotypes and passage numbers using a two-way analysis of variance (ANOVA) with Bonferroni or Sidak multiple comparisons test. The Shapiro-Wilk test was performed to test for normality. All statistical analyses were performed using GraphPad Prism 9.3.1 (GraphPad Software, La Jolla, CA) unless specified otherwise. Statistical significance was set at $\alpha = 0.05$. Data are shown as mean $\pm$ standard error of the mean (SEM).

References

1. McCormick, Anna; Fleming, Douglas; Charlton, J. Pain in the hand and wrist Assessing health needs in primary care Morbidity study from general practice. *BMJ* **310,** 1995 (1995).
2. Galatz, L. M., Ball, C. M., Teefey, S. A., Middleton, W. D. & Yamaguchi, K. The Outcome and Repair Integrity of Completely Arthroscopically Repaired Large and Massive Rotator Cuff Tears. *Journal of Bone and Joint Surgery - Series A* **86,** 219–224 (2004).

1032 3. Yang, G., Rothrauff, B. B. & Tuan, R. S. Tendon and ligament regeneration and repair:
1033 Clinical relevance and developmental paradigm. *Birth Defects Research Part C - Embryo*
1034 *Today: Reviews* **99,** 203–222 (2013).
1035 4. Andarawis-Puri, N., Flatow, E. L. & Soslowsky, L. J. Tendon basic science: Development,
1036 repair, regeneration, and healing. *Journal of Orthopaedic Research* **33,** 780–784 (2015).
1037 5. Le, A. D. K., Enweze, L., DeBaun, M. R. & Dragoo, J. L. Current Clinical Recommendations
1038 for Use of Platelet-Rich Plasma. *Current Reviews in Musculoskeletal Medicine* **11,** 624–634
1039 (2018).
1040 6. Kearney, R. S. *et al.* Effect of Platelet-Rich Plasma Injection vs Sham Injection on Tendon
1041 Dysfunction in Patients with Chronic Midportion Achilles Tendinopathy: A Randomized
1042 Clinical Trial. *JAMA - Journal of the American Medical Association* **326,** 137–144 (2021).
1043 7. Bedelbaeva, K. *et al.* Lack of p21 expression links cell cycle control and appendage
1044 regeneration in mice. *Proceedings of the National Academy of Sciences of the United States of*
1045 *America* **107,** 5845–5850 (2010).
1046 8. Rai, M. F. & Sandell, L. J. Regeneration of articular cartilage in healer and non-healer mice.
1047 *Matrix Biology* **39,** 50–55 (2014).
1048 9. Sereysky, J. B., Flatow, E. L. & Andarawis-Puri, N. Musculoskeletal regeneration and its
1049 implications for the treatment of tendinopathy. *International Journal of Experimental*
1050 *Pathology* **94,** 293–303 (2013).
1051 10. Lalley, A. L. *et al.* Improved biomechanical and biological outcomes in the MRL/MpJ murine
1052 strain following a full-length patellar tendon injury. *Journal of Orthopaedic Research* **33,**
1053 1693–1703 (2015).
1054 11. Paredes, J., Shiovitz, D. A., Andarawis-puri, N. & Sinai, M. Uncorrelated healing response of
1055 tendon and ear injuries in MRL highlight a role for the local tendon environment in driving
1056 scarless healing. *Connective Tissue Research* **59,** 472–482 (2018).

1057 12. Paredes, J., Marvin, J. C., Vaughn, B. & Andarawis-Puri, N. Innate tissue properties drive
1058 improved tendon healing in MRL/MpJ and harness cues that enhance behavior of canonical
1059 healing cells. *FASEB Journal* **34,** 8341–8356 (2020).
1060 13. George, N. S., Bell, R., Paredes, J. J., Taub, P. J. & Andarawis-Puri, N. Superior mechanical
1061 recovery in male and female MRL/MpJ tendons is associated with a unique genetic profile.
1062 *Journal of Orthopaedic Research* **39,** 1344–1354 (2021).
1063 14. Kallenbach, J. G. *et al.* Altered TGFB1 regulated pathways promote accelerated tendon
1064 healing in the superhealer MRL/MpJ mouse Short Title: Differential Transcriptional
1065 Regulation of Tendon Healing in MRL Mouse. *Scientific Reports* **12,** 2021.02.08.430308
1066 (2022).
1067 15. Chatterjee, M., Acosta, A., Taub, P. J. & Andarawis-Puri, N. Enhanced healing outcomes in
1068 MRL/MpJ mouse tissues conserved in insertion site following surgical repair. *Journal of*
1069 *Shoulder and Elbow Surgery* **31,** e593–e602 (2022).
1070 16. Paredes, J., Pekmezian, A. & Andarawis-Puri, N. MRL/MpJ tendon matrix-derived
1071 therapeutic promotes improved healing outcomes in scar-mediated canonical tendon healing.
1072 *Journal of Orthopaedic Research* 1–13 (2020). doi:10.1002/jor.24754
1073 17. Svitkina, T. The actin cytoskeleton and actin-based motility. *Cold Spring Harbor*
1074 *Perspectives in Biology* **10,** (2018).
1075 18. Geiger, B., Spatz, J. P. & Bershadsky, A. D. Environmental sensing through focal adhesions.
1076 *Nature Reviews Molecular Cell Biology* **10,** 21–33 (2009).
1077 19. Parsons, J. T., Horwitz, A. R. & Schwartz, M. A. Cell adhesion: Integrating cytoskeletal
1078 dynamics and cellular tension. *Nature Reviews Molecular Cell Biology* **11,** 633–643 (2010).
1079 20. Thievessen, I. *et al.* Vinculin-actin interaction couples actin retrograde flow to focal
1080 adhesions, but is dispensable for focal adhesion growth. *Journal of Cell Biology* **202,** 163–
1081 177 (2013).

1082 21. Jansen, K. A., Atherton, P. & Ballestrem, C. Mechanotransduction at the cell-matrix interface.
1083 *Seminars in Cell and Developmental Biology* **71,** 75–83 (2017).
1084 22. Dupont, S. *et al.* Role of YAP/TAZ in mechanotransduction. *Nature* **474,** 179–184 (2011).
1085 23. Wada, K. I., Itoga, K., Okano, T., Yonemura, S. & Sasaki, H. Hippo pathway regulation by
1086 cell morphology and stress fibers. *Development* **138,** 3907–3914 (2011).
1087 24. Driscoll, T. P., Cosgrove, B. D., Heo, S. J., Shurden, Z. E. & Mauck, R. L. Cytoskeletal to
1088 Nuclear Strain Transfer Regulates YAP Signaling in Mesenchymal Stem Cells. *Biophysical*
1089 *Journal* **108,** 2783–2793 (2015).
1090 25. Nardone, G. *et al.* YAP regulates cell mechanics by controlling focal adhesion assembly.
1091 *Nature Communications* **8,** (2017).
1092 26. Danen, E. H. J., Sonneveld, P., Brakebusch, C., Fässler, R. & Sonnenberg, A. The
1093 fibronectin-binding integrins α5β1 and αvβ3 differentially modulate RhoA-GTP loading,
1094 organization of cell matrix adhesions, and fibronectin fibrillogenesis. *Journal of Cell Biology*
1095 **159,** 1071–1086 (2002).
1096 27. Wierzbicka-Patynowski, I. & Schwarzbauer, J. E. The ins and outs of fibronectin matrix
1097 assembly. *Journal of Cell Science* **116,** 3269–3276 (2003).
1098 28. Ilić, D. *et al.* FAK promotes organization of fibronectin matrix and fibrillar adhesions.
1099 *Journal of Cell Science* **117,** 177–187 (2004).
1100 29. Filigheddu, N. *et al.* Fibronectin Matrix Assembly Requires Distinct Contributions from Rho
1101 Kinases I and -II. *Molecular biology of the cell* **18,** 986–994 (2007).
1102 30. Wang, E. Senescent Human Fibroblasts Resist Programmed Cell Death, and Failure to
1103 Suppress bell Is Involved. *Cancer Research* **55,** 2284–2292 (1995).
1104 31. Sasaki, M., Kumazaki, T., Takano, H., Nishiyama, M. & Mitsui, Y. Senescent cells are
1105 resistant to death despite low Bcl-2 level. *Mechanisms of Ageing and Development* **122,**
1106 1695–1706 (2001).

1107 32. Bedelbaeva, K. *et al.* Lack of p21 expression links cell cycle control and appendage
1108 regeneration in mice. *Proceedings of the National Academy of Sciences of the United States of*
1109 *America* **107,** 5845–5850 (2010).
1110 33. Jablonski, C. L., Besler, B. A., Ali, J. & Krawetz, R. J. p21−/− Mice Exhibit Spontaneous
1111 Articular Cartilage Regeneration Post-Injury. *Cartilage* **13,** 1608S-1617S (2021).
1112 34. Byron, A., Humphries, J. D. & Humphries, M. J. Defining the extracellular matrix using
1113 proteomics. *International Journal of Experimental Pathology* **94,** 75–92 (2013).
1114 35. Gwam, C., Mohammed, N. & Ma, X. Stem cell secretome, regeneration, and clinical
1115 translation: a narrative review. *Annals of Translational Medicine* **9,** 70–70 (2021).
1116 36. Warden, S. J. Animal models for the study of tendinopathy. *British Journal of Sports*
1117 *Medicine* **41,** 232–240 (2007).
1118 37. Hast, M. W., Zuskov, A. & Soslowsky, L. J. The role of animal models in tendon research.
1119 *Bone and Joint Research* **3,** 193–202 (2014).
1120 38. Badylak, S. F., Freytes, D. O. & Gilbert, T. W. Extracellular matrix as a biological scaffold
1121 material: Structure and function. *Acta Biomaterialia* **5,** 1–13 (2009).
1122 39. Hussey, G. S., Dziki, J. L. & Badylak, S. F. Extracellular matrix-based materials for
1123 regenerative medicine. *Nature Reviews Materials* 1 (2018). doi:10.1038/s41578-018-0023-x
1124 40. L., P. K. *et al.* The mesenchymal stem cell secretome: A new paradigm towards cell-free
1125 therapeutic mode in regenerative medicine. *Cytokine and Growth Factor Reviews* **46,** 1–9
1126 (2019).
1127 41. Zhang, Y. *et al.* Drug-induced regeneration in adult mice. **7,** (2015).
1128 42. Grinstein, M. *et al.* A quiescent resident progenitor pool is the central organizer of tendon
1129 healing. *bioRxiv* 1–62 (2022). doi:10.1101/2022.02.02.478533

1130 43. Poulsen, R. C. *et al.* Glucocorticoids induce senescence in primary human tenocytes by
1131 inhibition of sirtuin 1 and activation of the p53/p21 pathway: In vivo and in vitro evidence.
1132 *Annals of the Rheumatic Diseases* **73,** 1405–1413 (2014).
1133 44. Chen, M. *et al.* AQP1 modulates tendon stem/progenitor cells senescence during tendon
1134 aging. *Cell Death and Disease* **11,** (2020).
1135 45. Wang, C. *et al.* Inhibition of IKKβ/NF-κB signaling facilitates tendinopathy healing by
1136 rejuvenating inflamm-aging induced tendon-derived stem/progenitor cell senescence.
1137 *Molecular Therapy - Nucleic Acids* **27,** 562–576 (2022).
1138 46. Stowe, E. J., Keller, M. R. & Connizzo, B. K. Cellular Senescence Impairs Tendon
1139 Extracellular Matrix Remodeling in Response to Mechanical Unloading. Preprint at
1140 https://doi.org/10.1101/2023.12.22.572594 (2023)
1141 47. Basisty, N. *et al.* A Proteomic Atlas of Senescence-Associated Secretomes for Aging
1142 Biomarker Development. *SSRN Electronic Journal* 1–26 (2019). doi:10.2139/ssrn.3380253
1143 48. Da Silva-Álvarez, S. *et al.* Cell senescence contributes to tissue regeneration in zebrafish.
1144 *Aging Cell* **19,** 1–5 (2020).
1145 49. Antelo-Iglesias, L., Picallos-Rabina, P., Estévez-Souto, V., Da Silva-Álvarez, S. & Collado,
1146 M. The role of cellular senescence in tissue repair and regeneration. *Mechanisms of Ageing*
1147 *and Development* **198,** (2021).
1148 50. Jeon, O. H. *et al.* Local clearance of senescent cells attenuates the development of post-
1149 traumatic osteoarthritis and creates a pro-regenerative environment. *Nature Medicine* **23,**
1150 775–781 (2017).
1151 51. Wan, M., Gray-Gaillard, E. F. & Elisseeff, J. H. Cellular senescence in musculoskeletal
1152 homeostasis, diseases, and regeneration. *Bone Research* **9,** 1–12 (2021).

1153 52. Alisafaei, A. F., Shakiba, D., Iannucci, L. E. & Matthew, D. Tension anisotropy drives
1154 phenotypic transitions of cells via two-way cell-ECM feedback. *bioRxiv* 1–15 (2022).
1155 doi:10.1101/2022.03.13.484154
1156 53. Izu, Y. *et al.* Collagen XII mediated cellular and extracellular mechanisms regulate
1157 establishment of tendon structure and function. *Matrix Biology* **95,** 52–67 (2021).
1158 54. Banes, A. J. *et al.* Gap junctions regulate responses of tendon cells ex vivo to mechanical
1159 loading. *Clinical Orthopaedics and Related Research* **367,** 356–370 (1999).
1160 55. Waggett, A. D., Benjamin, M. & Ralphs, J. R. Connexin 32 and 43 gap junctions
1161 differentially modulate tenocyte response to cyclic mechanical load. *European Journal of*
1162 *Cell Biology* **85,** 1145–1154 (2006).
1163 56. Theodossiou, S. K., Murray, J. B. & Schiele, N. R. Cell-cell junctions in developing and adult
1164 tendons. *Tissue Barriers* **8,** (2020).
1165 57. Kubow, K. E. *et al.* Mechanical forces regulate the interactions of fibronectin and collagen i
1166 in extracellular matrix. *Nature Communications* **6,** (2015).
1167 58. Barker, T. H., Engler, A. J. & Jolla, L. The provisional matrix: setting the stage for tissue
1168 repair outcomes. *Matrix Biology* 1–4 (2018). doi:10.1016/j.matbio.2017.04.003.The
1169 59. Howell, K. *et al.* Novel Model of Tendon Regeneration Reveals Distinct Cell Mechanisms
1170 Underlying Regenerative and Fibrotic Tendon Healing. *Scientific Reports* **7,** 1–14 (2017).
1171 60. Best, K. T. & Loiselle, A. E. Scleraxis lineage cells contribute to organized bridging tissue
1172 during tendon healing and identify a subpopulation of resident tendon cells. *FASEB Journal*
1173 **33,** 8578–8587 (2019).
1174 61. Best, K. T. *et al.* NF-κB activation persists into the remodeling phase of tendon healing and
1175 promotes myofibroblast survival. *Science Signaling* **13,** (2020).
1176 62. Bi, Y. *et al.* Identification of tendon stem/progenitor cells and the role of the extracellular
1177 matrix in their niche. *Nature Medicine* **13,** 1219–1227 (2007).

1178 63. Valekova, I., Skalnikova, H. K., Jarkovska, K., Motlik, J. & Kovarova, H. in *Stem Cell*
1179 *Renewal and Cell-Cell Communication. Methods in Molecular Biology* (ed. Turksen, K.)
1180 **1212,** 39–63 (2014).
1181 64. Marvin, J. C., Brakewood, M. E., Poon, M. L. S. & Andarawis-Puri, N. Regenerative
1182 MRL/MpJ tendon cells exhibit sex differences in morphology, proliferation,
1183 mechanosensitivity, and cell–ECM organization. *Journal Orthopaedic Research* **41,** 2273–
1184 2286 (2023).
1185 65. Cho, Y. *et al.* CTRP3 exacerbates tendinopathy by dysregulating tendon stem cell
1186 differentiation and altering extracellular matrix composition. *Science Advances* **7,** (2021).
1187 66. Rovai, L. E., Herschman, H. R. & Smith, J. B. The murine neutrophil-chemoattractant
1188 chemokines LIX, KC, and MIP-2 have distinct induction kinetics, tissue distributions, and
1189 tissue-specific sensitivities to glucocorticoid regulation in endotoxemia. *Journal of Leukocyte*
1190 *Biology* **64,** 494–502 (1998).
1191 67. Ohtsuka, Y., Lee, J., Stamm, D. S. & Sanderson, I. R. MIP-2 secreted by epithelial cells
1192 increases neutrophil and lymphocyte recruitment in the mouse intestine. *Gut* **49,** 526–533
1193 (2001).
1194 68. Zins, S. R., Amare, M. F., Anam, K., Elster, E. A. & Davis, T. A. Wound trauma mediated
1195 inflammatory signaling attenuates a tissue regenerative response in MRL/MpJ mice. *Journal*
1196 *of Inflammation* **7,** 1–9 (2010).
1197 69. Song, J., Wu, C., Zhang, X. & Sorokin, L. M. In Vivo Processing of CXCL5 (LIX) by Matrix
1198 Metalloproteinase (MMP)-2 and MMP-9 Promotes Early Neutrophil Recruitment in IL-1β–
1199 Induced Peritonitis. *The Journal of Immunology* **190,** 401–410 (2013).
1200 70. Plant, T. *et al.* Semaphorin 3F signaling actively retains neutrophils at sites of inflammation.
1201 *Journal of Clinical Investigation* **130,** 3221–3237 (2020).

1202 71. Tarafder, S. *et al.* Tendon stem/progenitor cells regulate inflammation in tendon healing via
1203 JNK and STAT3 signaling. *FASEB Journal* **31,** 3991–3998 (2017).
1204 72. Seternes, O. M., Kidger, A. M. & Keyse, S. M. Dual-specificity MAP kinase phosphatases in
1205 health and disease. *Biochimica et Biophysica Acta - Molecular Cell Research* **1866,** 124–143
1206 (2019).
1207 73. Blache, U. *et al.* Inhibition of ERK 1/2 kinases prevents tendon matrix breakdown. *Scientific*
1208 *Reports* **11,** (2021).
1209 74. Marvin, J. C., Mochida, A., Paredes, J., Vaughn, B. & Andarawis-Puri, N. Detergent-Free
1210 Decellularization Preserves the Mechanical and Biological Integrity of Murine Tendon.
1211 *Tissue Engineering Part C: Methods* **28,** 646–655 (2022).
1212 75. Wipff, P. J. *et al.* The covalent attachment of adhesion molecules to silicone membranes for
1213 cell stretching applications. *Biomaterials* **30,** 1781–1789 (2009).
1214 76. Kuddannaya, S. *et al.* Surface chemical modification of poly(dimethylsiloxane) for the
1215 enhanced adhesion and proliferation of mesenchymal stem cells. *ACS Applied Materials and*
1216 *Interfaces* **5,** 9777–9784 (2013).
1217 77. Gannier, F., White, E., Lacampagne, A., Garnier, D. & Guennec, J.-Y. Le. Streptomycin
1218 reverses a large stretch induced increase in [Ca"'], in isolated guinea pig ventricular
1219 myocytes. *Cardiovascular Research* **28,** 1193–1198 (1994).
1220 78. Metsalu, T. & Vilo, J. ClustVis: A web tool for visualizing clustering of multivariate data
1221 using Principal Component Analysis and heatmap. *Nucleic Acids Research* **43,** W566–W570
1222 (2015).
1223 79. Horzum, U., Ozdil, B. & Pesen-Okvur, D. Step-by-step quantitative analysis of focal
1224 adhesions. *MethodsX* **1,** 56–59 (2014).
1225 80. Fonck, E. *et al.* Effect of aging on elastin functionality in human cerebral arteries. *Stroke* **40,**
1226 2552–2556 (2009).

Acknowledgments

We acknowledge K. Adebowale for assistance and insightful feedback in interpreting the single-cell actin cytoskeleton and focal adhesion data. We acknowledge C. Mendias and A. Shimpi for helpful discussions in interpreting the proteomics data. We also acknowledge Y. Wang for access to their lyophilizer. We acknowledge R. Bell and M. Pacheco for their contributions in developing the recombinant protein panel. We acknowledge E. Maloney for performing rat tenocyte isolations. We also acknowledge the Cornell Center for Animal Resources and Education (CARE) staff for animal care. All graphical schematics and illustrations were generated using BioRender.

Funding: This project was funded by: National Institutes of Health (NIH) and National Science Foundation (NSF).

NIH Grant R01AR068301 (NAP)
NIH Grant R21AR074602 (NAP)
NIH Grant R56AR077239 (NAP)
NIH Grant 1S10RR025502 (Cornell University Biotechnology Resource Center)
NSF GRFP DGE-1650441 (JCM)

Author contributions: https://www.elsevier.com/authors/policies-and-guidelines/credit-author-statement

Conceptualization: JCM, NAP
Methodology: JCM, NAP
Investigation: JCM, EJL, HC
Visualization: JCM, EJL, HC
Supervision: NAP
Writing—original draft: JCM
Writing—review & editing: JCM, NAP

JCM and NAP conceived the study and developed the hypotheses. JCM designed experiments and performed all protocol development, animal surgeries, and research. JCM and EJL carried out proteomics analyses and confocal microscopy experiments. JCM, EJL, and HC analyzed immunofluorescence and staining data. NAP supervised the work. JCM wrote the paper. JCM and NAP edited and revised the manuscript.

Competing interests: The authors declare that they have no competing interests.

Data and materials availability: All data are available in the main text or the supplementary materials. Raw data for all Quantibody experiments will be made publicly available for access upon publication.

Figures and Tables

Fig. 1. MRL/MpJ tenocytes demonstrate enhanced mechanosensitivity and cell migration and form more actin-rich, axon-like cellular protrusions compared to B6 tenocytes. (**A**) Experimental design to assess characterize morphology and focal adhesion formation. (**B to E**) IF staining of F-actin (gray) and vinculin (green) of B6 and MRL/MpJ tenocytes cultured on collagen I-coated substrates (scale bar, 100 μm; 2X-magnified insets in the top-right corner of representative vinculin images). MRL/MpJ tenocytes formed more extensive cellular protrusions

1277 (C) that were accompanied by greater cell spreading and perimeter (D) and
1278 assembly of nascent focal adhesions compared to B6 tenocytes (E). (**F to H**)
1279 Experimental design to quantify tenocyte migration via wound scratch assays.
1280 Wound scratch analysis (F) showed that a significantly greater number of
1281 MRL/MpJ tenocytes than B6 tenocytes migrated on fibronectin-coated substrates
1282 after 12 hours post-scratch (G) despite comparable cell protrusion characteristics
1283 between cells cultured on collagen I and fibronectin (H). (**I**) Experimental design
1284 to assess YAP-mediated mechanosignaling. IF staining of phalloidin (grey) and
1285 YAP (magnified 3X in gray; green in merged representative images) of B6 and
1286 MRL/MpJ tenocytes cultured on collagen I-coated substrates (scale bar, 100 μm)
1287 with pharmacological inhibitors for actin polymerization (Lat-A), myosin II
1288 (blebbistatin), and ROCK (Y-27632). DMSO-treated cells served as a control. (**J**)
1289 At baseline, MRL/MpJ tenocytes displayed significantly higher YAP nuclear
1290 localization than B6 tenocytes. (**K**) Relative nuclear translocation of YAP
1291 (normalized to respective DMSO control mean) was significantly reduced in
1292 MRL/MpJ tenocytes compared to B6 tenocytes with inhibition of myosin II and
1293 ROCK. *$P < 0.05$, **$P < 0.01$, ***$P < 0.001$, ****$P < 0.0001$. Significance was
1294 determined using a Welch's t-test when comparing B6 and MRL/MpJ tenocytes, or
1295 a two-way ANOVA with post-hoc Bonferroni when comparing genotypes for each
1296 inhibitor for YAP data. Representative images shown for all staining experiments.

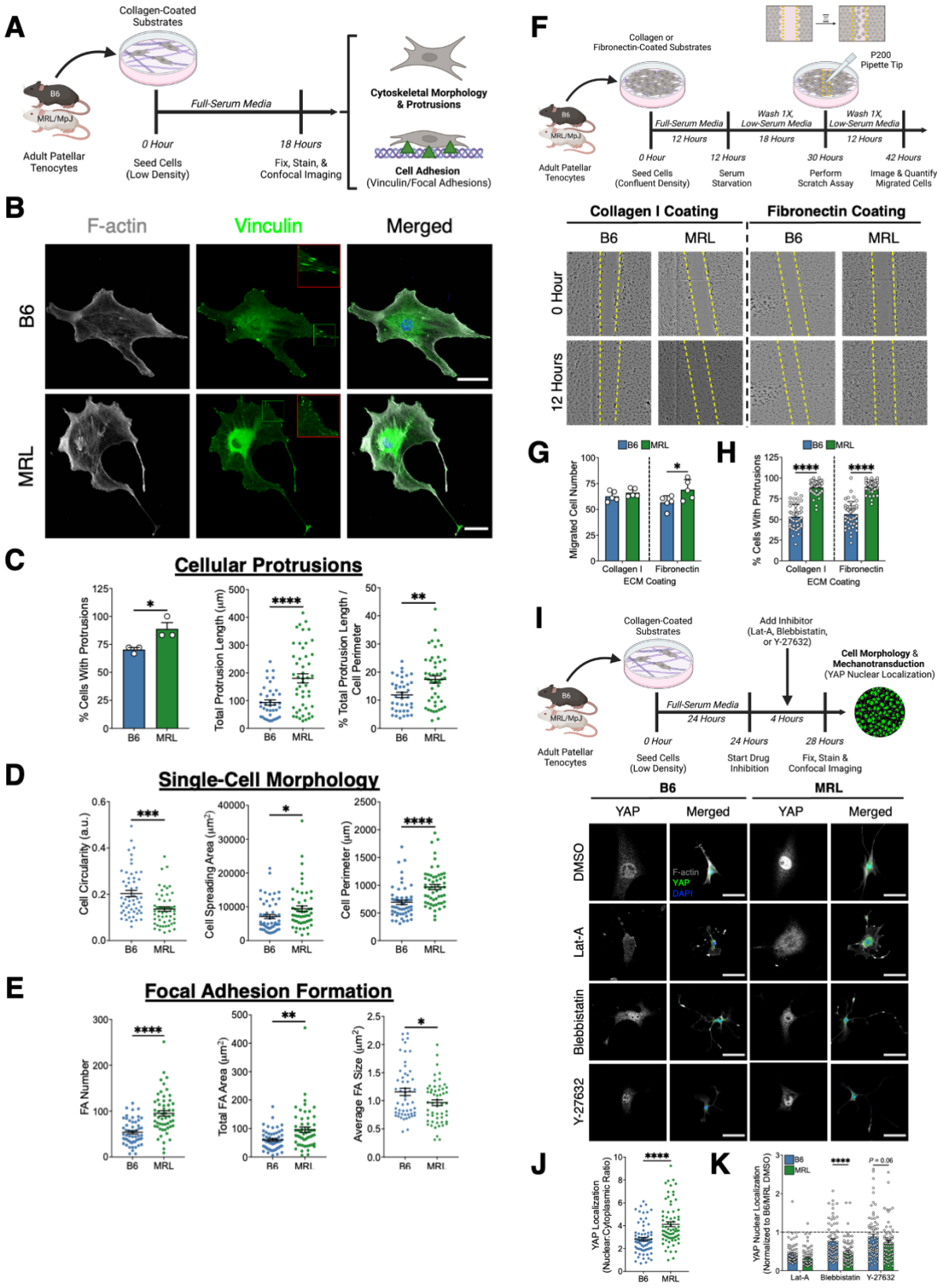
A
Collagen-Coated Substrates
B6
MRL/MpJ
Adult Patellar Tenocytes
Full-Serum Media
0 Hour
Seed Cells (Low Density)
18 Hours
Fix, Stain, & Confocal Imaging
Cytoskeletal Morphology & Protrusions
Cell Adhesion (Vinculin/Focal Adhesions)
B
F-actin
Vinculin
Merged
B6
MRL
C
Cellular Protrusions
% Cells With Protrusions
Total Protrusion Length (μm)
% Total Protrusion Length / Cell Perimeter
D
Single-Cell Morphology
Cell Circularity (a.u.)
Cell Spreading Area (μm²)
Cell Perimeter (μm)
E
Focal Adhesion Formation
FA Number
Total FA Area (μm²)
Average FA Size (μm²)
F
Collagen or Fibronectin-Coated Substrates
P200 Pipette Tip
Full-Serum Media
12 Hours
Wash 1X, Low-Serum Media
18 Hours
Wash 1X, Low-Serum Media
12 Hours
0 Hour
Seed Cells (Confluent Density)
12 Hours
Serum Starvation
30 Hours
Perform Scratch Assay
42 Hours
Image & Quantify Migrated Cells
Collagen I Coating
Fibronectin Coating
0 Hour
12 Hours
G
Migrated Cell Number
Collagen I
Fibronectin
ECM Coating
H
% Cells With Protrusions
I
Add Inhibitor (Lat-A, Blebbistatin, or Y-27632)
Cell Morphology & Mechanotransduction (YAP Nuclear Localization)
Full-Serum Media
24 Hours
4 Hours
24 Hours
Start Drug Inhibition
28 Hours
Fix, Stain & Confocal Imaging
YAP
Merged
DMSO
Lat-A
Blebbistatin
Y-27632
F-actin
DAPI
J
YAP Localization (Nuclear:Cytoplasmic Ratio)
K
YAP Nuclear Localization (Normalized to B6/MRL DMSO)
P = 0.06

1299 **Fig. 2. MRL/MpJ tenocytes promote cytoskeletal and cellular alignment, ECM**
1300 **deposition, and intercellular communication consisted with effective tendon**
1301 **healing outcomes *in vivo*.** (**A**) Experimental design to assess confluent tenocyte
1302 behavior after 7 days of culture in full-serum media. (**B to D**) IF staining of (B)
1303 connexin-43 (Cx-43, green) and F-actin (grey) in addition to (C) fibronectin
1304 (green), collagen I (cyan), and αSMA (gray) in confluent B6 and MRL/MpJ
1305 tenocytes (scale bar, 100 μm). MRL/MpJ tenocytes displayed greater cytoskeletal
1306 and matrix anisotropy, ECM fibrillogenesis, and arrangement of nuclei in linear
1307 arrays (indicated by the dashed yellow line) compared to B6 tenocytes. (**D to F**)
1308 MRL/MpJ tenocytes exhibited significantly greater F-actin and fibronectin
1309 coherency/alignment (D), fibronectin and collagen I deposition (E), and cell
1310 number and Cx-43 levels (F) than B6 tenocytes. (**G**) IF staining of Cx-43 (green)
1311 and F-actin (grey) at moderate cell densities after 3 days of culture revealed that
1312 gap junctions localize along the length and tips of actin-rich cellular protrusions
1313 (indicated by yellow arrowheads) to facilitate intercellular communication. (**H**)
1314 αSMA expression remained comparable between B6 and MRL/MpJ tenocytes
1315 after 3 and 7 days of culture suggesting that increased myofibroblast activation
1316 does not drive improved structural organization *in vitro*. *$P < 0.05$, **$P < 0.01$,
1317 ***$P < 0.001$, ****$P < 0.0001$. Significance was determined using a Welch's t-test
1318 when comparing coherency, ECM thickness, or cell number data. Integrated
1319 density data on a per cell basis further normalized to the B6 mean was compared
1320 using a non-parametric Mann-Whitney *U* test. Representative images shown for all
1321 staining experiments.
1322
1323
1324

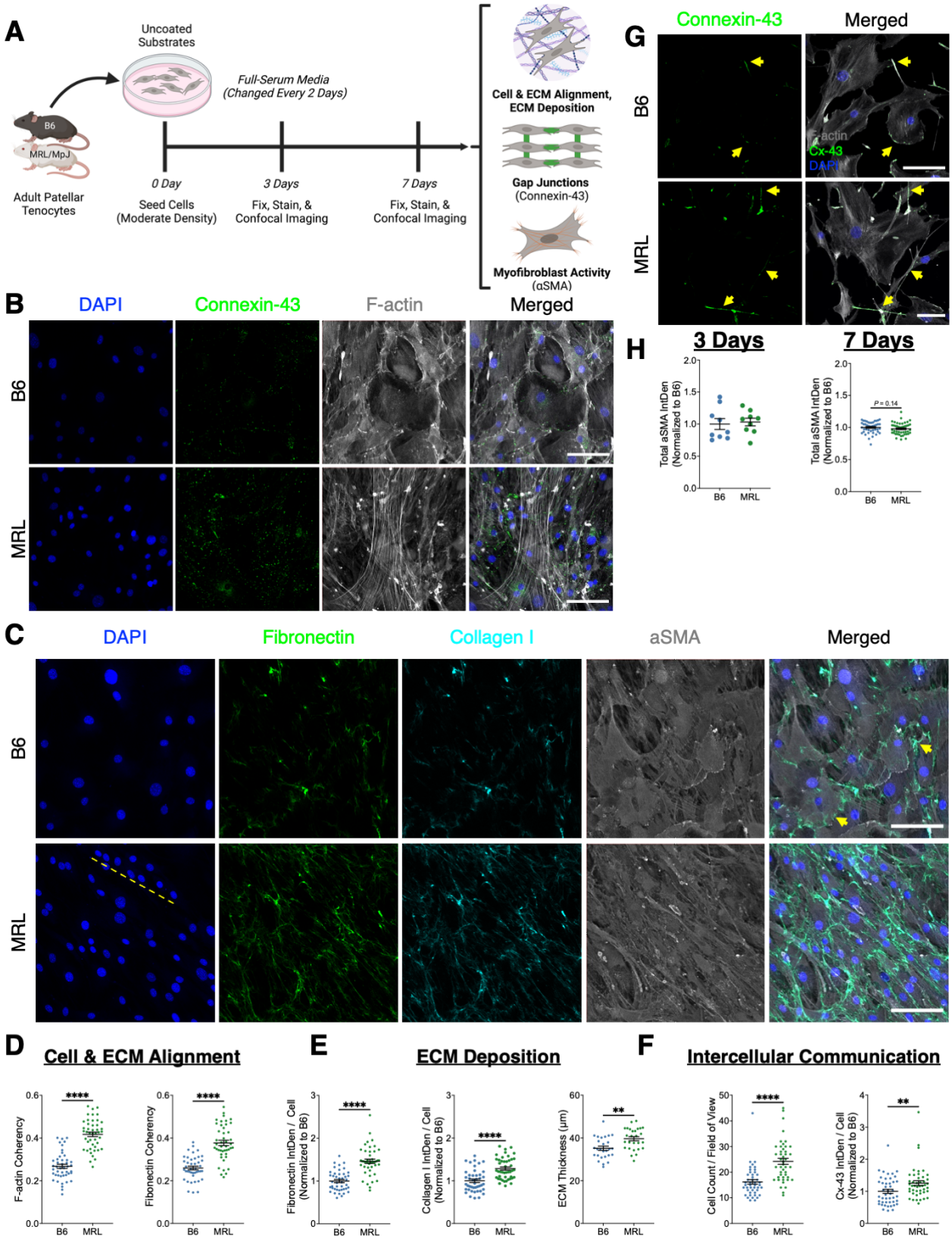
A
Uncoated Substrates
Full-Serum Media (Changed Every 2 Days)
B6
MRL/MpJ
Adult Patellar Tenocytes
0 Day
Seed Cells (Moderate Density)
3 Days
Fix, Stain, & Confocal Imaging
7 Days
Fix, Stain, & Confocal Imaging
Cell & ECM Alignment, ECM Deposition
Gap Junctions (Connexin-43)
Myofibroblast Activity (αSMA)
B
DAPI
Connexin-43
F-actin
Merged
B6
MRL
C
DAPI
Fibronectin
Collagen I
aSMA
Merged
B6
MRL
G
Connexin-43
Merged
B6
MRL
F-actin
Cx-43
DAPI
H
3 Days
7 Days
Total aSMA IntDen (Normalized to B6)
P = 0.14
B6
MRL
D
Cell & ECM Alignment
F-actin Coherency
Fibronectin Coherency
E
ECM Deposition
Fibronectin IntDen / Cell (Normalized to B6)
Collagen I IntDen / Cell (Normalized to B6)
ECM Thickness (μm)
F
Intercellular Communication
Cell Count / Field of View
Cx-43 IntDen / Cell (Normalized to B6)
****
**

1326 **Fig. 3. Quantitative proteomics reveal biological signatures enriched in the**
1327 **MRL/MpJ tenocyte secretome that are conserved across static and dynamic**
1328 **culture compared to those of B6.** (**A**) Schematic illustration of primary mouse
1329 tenocyte secretome collection under static and dynamic culture conditions for
1330 RayBiotech quantitative proteomics analyses. (**B**) Breakdown of differentially
1331 expressed proteins (DEPs) upregulated in the B6 (in blue) and MRL/MpJ (in red)
1332 tenocyte secretomes. (**C**) Principal components analysis (PCA) showed distinct
1333 clustering of static secretome samples by genotype (left) but overlap of dynamic
1334 secretome samples (right). (**D and E**) Heat maps of Z-score hierarchical clustering
1335 based on Euclidean distance for rows and volcano plots of the static (D) and
1336 dynamic (E) secretomes. Blue and green bars underneath heat maps denote B6 and
1337 MRL/MpJ biological replicates, respectively. (**F to H**) Comparative ingenuity
1338 pathway analysis (IPA) of the static and dynamic secretomes predicted similar
1339 activation Z-score patterns for the top 10 diseases and functions (F) and canonical
1340 pathways (G) but contrasting activation states for 8 of 10 upstream regulators (H).
1341 (**I**) Heat map visualizing relative changes in protein concentration within each
1342 genotype for cytokine targets shared between the static and dynamic secretomes.
1343 Blue and red colors indicate annotations predicted to be activated or enriched in B6
1344 or MRL/MpJ secretomes, respectively. Black boxes indicate annotations or
1345 cytokines that were not detected.
1346

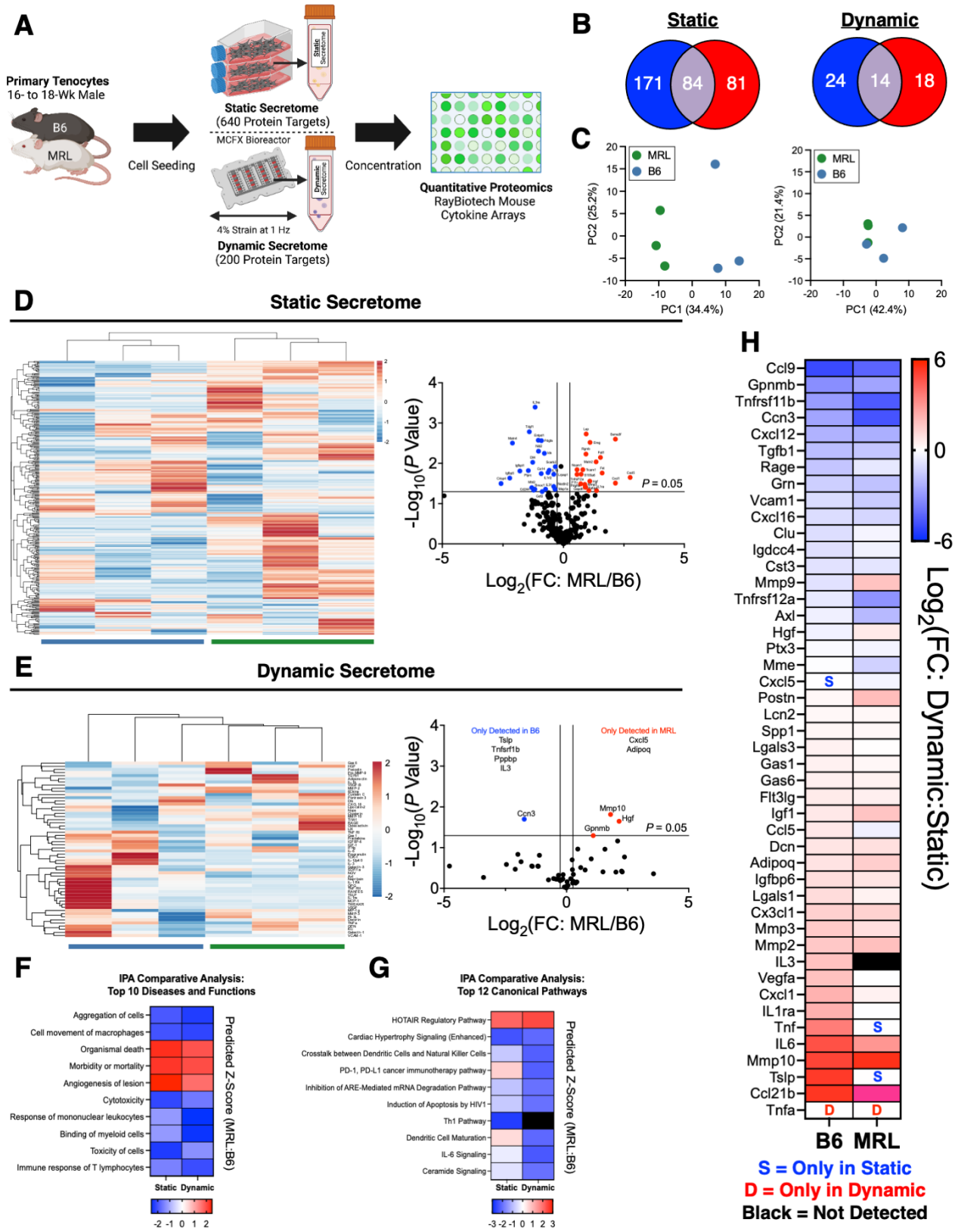
A
Primary Tenocytes
16- to 18-Wk Male
B6
MRL
Cell Seeding
Static Secretome
(640 Protein Targets)
MCFX Bioreactor
4% Strain at 1 Hz
Dynamic Secretome
(200 Protein Targets)
Concentration
Quantitative Proteomics
RayBiotech Mouse
Cytokine Arrays
B
Static
Dynamic
171
84
81
24
14
18
C
MRL
B6
PC2 (25.2%)
PC1 (34.4%)
PC2 (21.4%)
PC1 (42.4%)
D
Static Secretome
-Log10(P Value)
Log2(FC: MRL/B6)
P = 0.05
E
Dynamic Secretome
Only Detected in B6
Tslp
Tnfsrf1b
Pppbp
IL3
Only Detected in MRL
Cxcl5
Adipoq
Ccn3
Mmp10
Hgf
Gpnmb
F
IPA Comparative Analysis:
Top 10 Diseases and Functions
Aggregation of cells
Cell movement of macrophages
Organismal death
Morbidity or mortality
Angiogenesis of lesion
Cytotoxicity
Response of mononuclear leukocytes
Binding of myeloid cells
Toxicity of cells
Immune response of T lymphocytes
Static
Dynamic
Predicted Z-Score (MRL:B6)
G
IPA Comparative Analysis:
Top 12 Canonical Pathways
HOTAIR Regulatory Pathway
Cardiac Hypertrophy Signaling (Enhanced)
Crosstalk between Dendritic Cells and Natural Killer Cells
PD-1, PD-L1 cancer immunotherapy pathway
Inhibition of ARE-Mediated mRNA Degradation Pathway
Induction of Apoptosis by HIV1
Th1 Pathway
Dendritic Cell Maturation
IL-6 Signaling
Ceramide Signaling
Static
Dynamic
Predicted Z-Score (MRL:B6)
H
Ccl9
Gpnmb
Tnfrsf11b
Ccn3
Cxcl12
Tgfb1
Rage
Grn
Vcam1
Cxcl16
Clu
Igdcc4
Cst3
Mmp9
Tnfrsf12a
Axl
Hgf
Ptx3
Mme
Cxcl5
Postn
Lcn2
Spp1
Lgals3
Gas1
Gas6
Flt3lg
Igf1
Ccl5
Dcn
Adipoq
Igfbp6
Lgals1
Cx3cl1
Mmp3
Mmp2
IL3
Vegfa
Cxcl1
IL1ra
Tnf
IL6
Mmp10
Tslp
Ccl21b
Tnfa
B6
MRL
Log2(FC: Dynamic:Static)
S = Only in Static
D = Only in Dynamic
Black = Not Detected

1353
1354 **Fig. 4. An adult population MRL/MpJ tenocytes undergo increased proliferative and**
1355 **apoptotic activity compared to B6 tenocytes**. (**A**) Experimental design to characterize
1356 cellular senescence and the growth kinetics of B6 and MRL/MpJ tenocytes. (**B and C**) B6
1357 tenocytes progressively accumulated ß-galactosidase (ß-gal) activity associated with
1358 cellular senescence in response to replicative stress induced by serial passages (P3-P5; B),
1359 whereas MRL/MpJ tenocytes maintained a non-senescent phenotype (C). (**D)** Population
1360 growth kinetics are diminished in B6 as compared to MRL/MpJ tenocytes at P5 as
1361 evidenced by significantly increased population doubling time (PDT) and decreased
1362 cumulative population doubling (CPD). (**E to G**) Immunohistochemical (IHC) staining of
1363 Ki-67 and cleaved caspase-3 found significantly increased cell proliferation (F) and
1364 apoptosis (G), respectively, in MRL/MpJ tendons compared to B6 tendons at 1 and 4
1365 weeks (F) after acute injury *in vivo* (scale bar, 50 µm; arrowheads indicate positively-
1366 stained cells; all sections were counterstained with toluidine blue). (**H**) Experimental
1367 design to measure DNA damage and p21 expression in B6 and MRL/MpJ tenocytes.
1368 Immunofluorescence (IF) staining revealed similar intrinsic expression of p21(green) and
1369 DNA damage (indicated by γH2AX-positive foci, magenta) between B6 and MRL/MpJ
1370 tenocytes (scale bar, 100 µm). $^{*}P < 0.05$, $^{**}P < 0.01$, $^{****}P < 0.0001$. Significance was
1371 determined using a two-way analysis of variance (ANOVA) with post-hoc Bonferroni or
1372 Šidák for *in vitro* assays, or an unpaired Student's t-test when comparing genotypes at
1373 each timepoint for IHC data. Representative images shown for all staining experiments.
1374

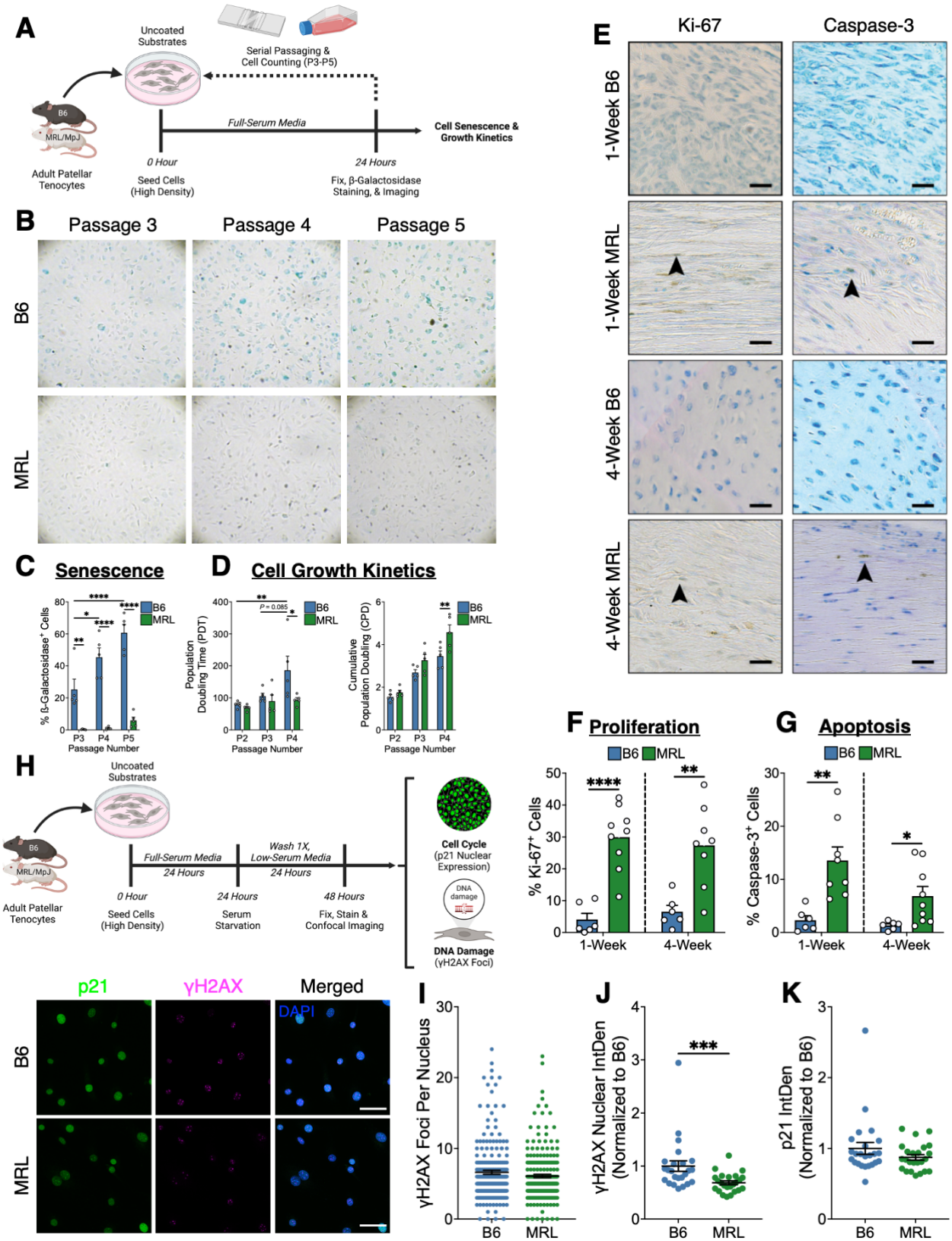
A
Uncoated Substrates
Serial Passaging & Cell Counting (P3-P5)
B6
MRL/MpJ
Adult Patellar Tenocytes
Full-Serum Media
Cell Senescence & Growth Kinetics
0 Hour
Seed Cells (High Density)
24 Hours
Fix, β-Galactosidase Staining, & Imaging
B
Passage 3
Passage 4
Passage 5
B6
MRL
C
Senescence
% β-Galactosidase+ Cells
B6
MRL
P3
P4
P5
Passage Number
D
Cell Growth Kinetics
Population Doubling Time (PDT)
P = 0.085
P2
P3
P4
Passage Number
Cumulative Population Doubling (CPD)
E
Ki-67
Caspase-3
1-Week B6
1-Week MRL
4-Week B6
4-Week MRL
F
Proliferation
% Ki-67+ Cells
1-Week
4-Week
G
Apoptosis
% Caspase-3+ Cells
H
Uncoated Substrates
Full-Serum Media
24 Hours
Wash 1X, Low-Serum Media
24 Hours
0 Hour
Seed Cells (High Density)
24 Hours
Serum Starvation
48 Hours
Fix, Stain & Confocal Imaging
Cell Cycle (p21 Nuclear Expression)
DNA damage
DNA Damage (γH2AX Foci)
p21
γH2AX
Merged
DAPI
I
γH2AX Foci Per Nucleus
J
γH2AX Nuclear IntDen (Normalized to B6)
K
p21 IntDen (Normalized to B6)

1377 **Fig. 5. B6 and MRL/MpJ tenocytes treated with a combination of MRL/MpJ-derived**
1378 **decellularized provisional ECM and secretome achieve comparable**
1379 **morphologies and cellular mechanotransduction**. (**A**) Experimental design and
1380 *in vitro* culture model of single-cell experiments for tenocytes cultured on dPECM
1381 with tenocyte-sourced secretome (henceforth referred to as 'components'). (**B**)
1382 Representative cell outlines of B6 and MRL/MpJ tenocytes cultured with B6 or
1383 MRL/MpJ-derived components (scale bar, 100 μm) to visualize cytoskeletal
1384 morphology and cellular protrusions. (**C**) IF staining of F-actin (grey) and vinculin
1385 (green) of treated B6 and MRL/MpJ tenocytes. (**D to F**) Cellular protrusion
1386 characteristics (D), single-cell morphological parameters (E), and focal adhesion
1387 profiles (F) are identical between B6 and MRL/MpJ tenocytes treated with
1388 MRL/MpJ-derived components and significantly different from B6 tenocytes
1389 treated with B6-derived components. (**g**) Representative cell outlines of B6
1390 tenocytes cultured with MRL/MpJ-derived components (scale bar, 200 μm). Cells
1391 with greater protrusion numbers and total protrusion lengths were associated with
1392 increased myofibroblast activity as visualized by dark blue colors indicating higher
1393 αSMA expression (relative to B6 mean). (**H and I**) MRL/MpJ-derived components
1394 promoted significantly greater αSMA expression (H) in B6 tenocytes but not cell
1395 proliferation (I) compared to B6-derived components or B6 cells cultured on
1396 collagen I-coated substrates. *$P < 0.05$, **$P < 0.01$, ***$P < 0.001$, ****$P <$
1397 0.0001. Significance was determined using a one-way Welch's ANOVA with post-
1398 hoc Games-Howell for cell morphology and focal adhesion data. For cellular
1399 protrusion data, significance was determined using a one-way ANOVA with post-
1400 hoc Tukey (percentage of cells with protrusions) or Kruskal-Wallis test with post-
1401 hoc Dunn's (number of protrusions and normalized total protrusion length).
1402 Representative images shown for all staining experiments.
1403
1404
1405

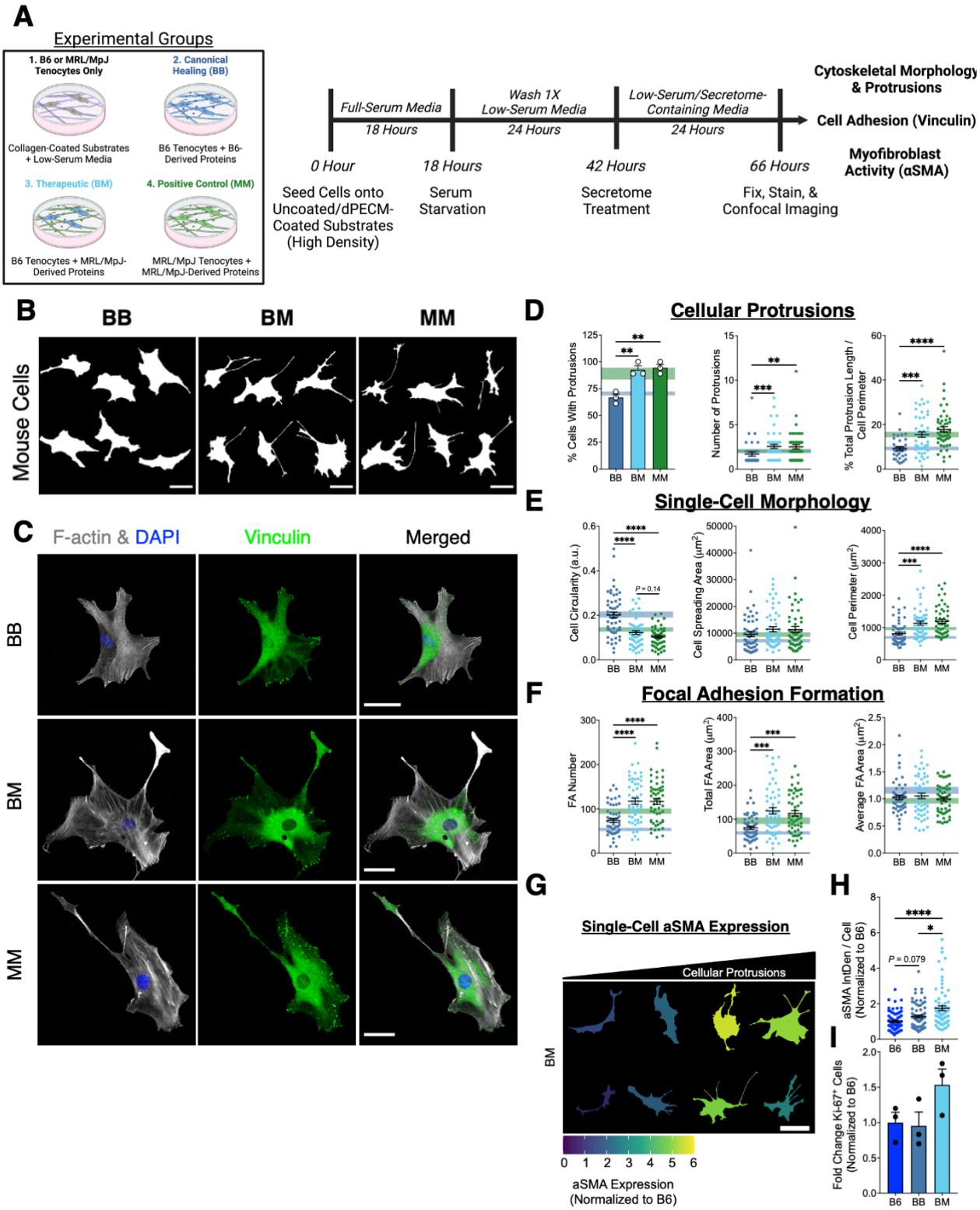
A
Experimental Groups
1. B6 or MRL/MpJ Tenocytes Only
2. Canonical Healing (BB)
Collagen-Coated Substrates + Low-Serum Media
B6 Tenocytes + B6-Derived Proteins
3. Therapeutic (BM)
4. Positive Control (MM)
B6 Tenocytes + MRL/MpJ-Derived Proteins
MRL/MpJ Tenocytes + MRL/MpJ-Derived Proteins
Full-Serum Media
18 Hours
Wash 1X Low-Serum Media
24 Hours
Low-Serum/Secretome-Containing Media
24 Hours
0 Hour
18 Hours
42 Hours
66 Hours
Seed Cells onto Uncoated/dPECM-Coated Substrates (High Density)
Serum Starvation
Secretome Treatment
Fix, Stain, & Confocal Imaging
Cytoskeletal Morphology & Protrusions
Cell Adhesion (Vinculin)
Myofibroblast Activity (αSMA)
B
BB
BM
MM
Mouse Cells
C
F-actin & DAPI
Vinculin
Merged
D
Cellular Protrusions
% Cells With Protrusions
Number of Protrusions
% Total Protrusion Length / Cell Perimeter
E
Single-Cell Morphology
Cell Circularity (a.u.)
Cell Spreading Area (μm²)
Cell Perimeter (μm²)
P = 0.14
F
Focal Adhesion Formation
FA Number
Total FA Area (μm²)
Average FA Area (μm²)
G
Single-Cell aSMA Expression
Cellular Protrusions
aSMA Expression (Normalized to B6)
H
aSMA IntDen / Cell (Normalized to B6)
P = 0.079
I
Fold Change Ki-67⁺ Cells (Normalized to B6)

1408 **Fig. 6. Combination of MRL/MpJ-derived components modulate confluent B6**
1409 **tenocytes toward an MRL/MpJ-like regenerative phenotype *in vitro*.** (**A**)
1410 Experimental design and *in vitro* culture model of confluent cell experiments for
1411 tenocytes cultured with mouse-derived components for 7 days. (**B**) MRL/MpJ
1412 tenocytes maintained significantly greater F-actin alignment and ECM deposition
1413 than B6 tenocytes under serum-deprived culture conditions. However, Cx-43
1414 levels were significantly downregulated in MRL/MpJ tenocytes compared to B6
1415 tenocytes. (**C**) IF staining of F-actin (grey), fibronectin (green), and Cx-43
1416 (magenta) of confluent B6 and MRL/MpJ tenocytes treated with only MRL/MpJ
1417 dPECM, only MRL/MpJ secretome, or a combination of mouse-derived
1418 components for 7 days (scale bar, 100 μm). A polygonal, epithelial cell-like
1419 morphology was observed in B6 tenocytes treated with B6-derived components
1420 (indicated by yellow arrowheads). (**D**) B6 and MRL/MpJ tenocytes treated with
1421 MRL/MpJ-derived components exhibited comparable F-actin alignment and
1422 fibronectin deposition that were significantly greater than those of B6 tenocytes
1423 treated with B6-derived components. However, both treated B6 tenocyte groups
1424 had significantly lower Cx-43 levels compared to MRL/MpJ tenocytes treated with
1425 MRL/MpJ-derived components. (**E**) There was a combined benefit of treating B6
1426 tenocytes with both the MRL/MpJ dPECM and secretome on F-actin alignment,
1427 fibronectin deposition, and Cx-43 levels compared to either component alone. (**F**)
1428 Experimental design to quantify cellular senescence in tenocytes cultured with
1429 mouse-derived components for 3 days. MRL/MpJ components were unable to
1430 attenuate the onset of B6 tenocyte senescence/accumulation of ß-gal activity after
1431 48 hours of treatment. (**G**) B6 tenocytes treated with MRL/MpJ-derived
1432 components displayed a smaller proportion of senescent cells due to significantly
1433 increased total cell number compared to either component alone as well as B6
1434 tenocytes treated with B6-derived components. *$P < 0.05$, **$P < 0.01$, ***$P <$
1435 0.001, ****$P < 0.0001$. Significance was determined using a one-way ANOVA
1436 with post-hoc Tukey. Representative images shown for all staining experiments.

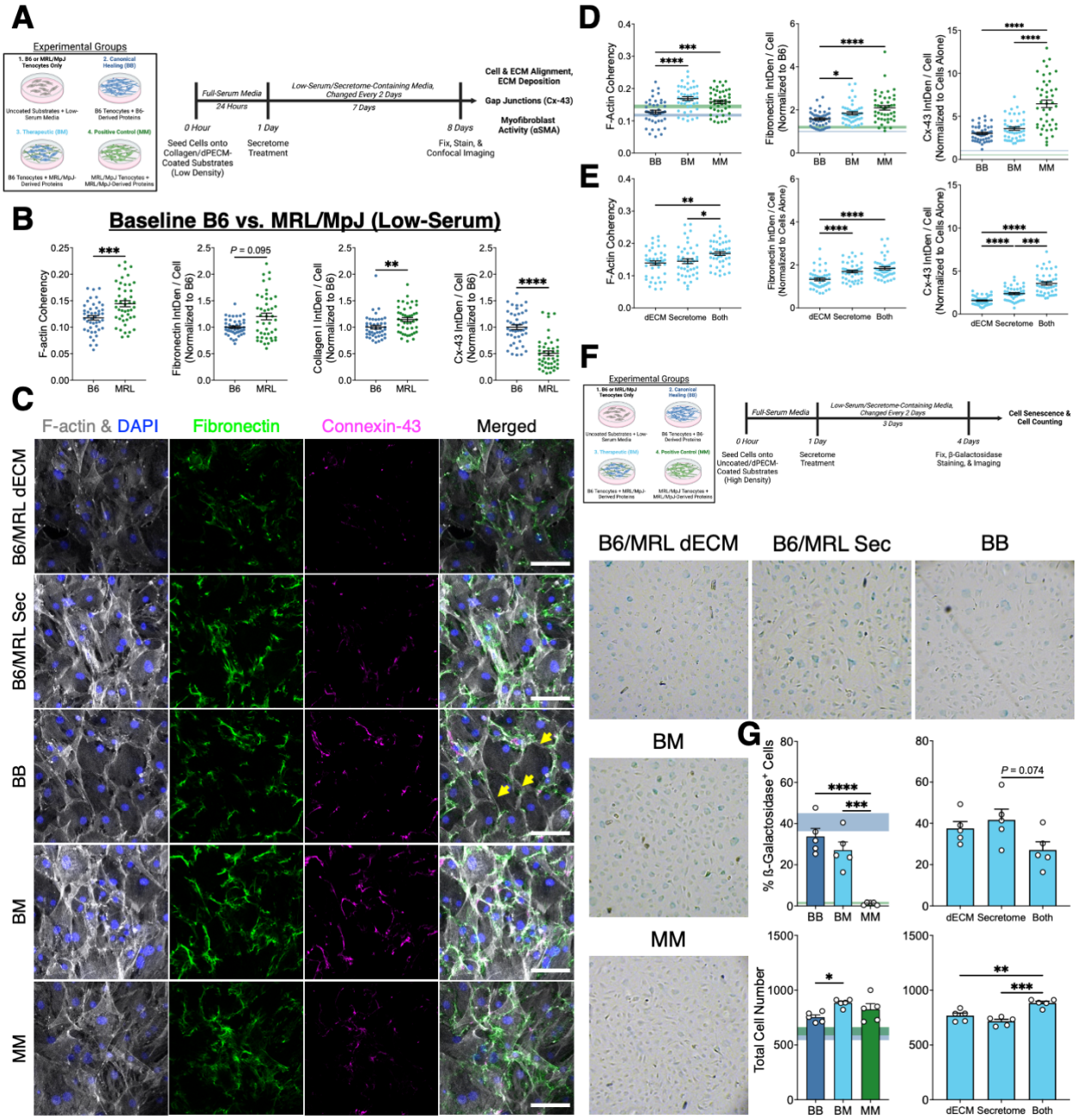
A
Experimental Groups
1. B6 or MRL/MpJ Tenocytes Only
2. Canonical Healing (BB)
3. Therapeutic (BM)
4. Positive Control (MM)
Uncoated Substrates + Low-Serum Media
B6 Tenocytes + B6-Derived Proteins
B6 Tenocytes + MRL/MpJ-Derived Proteins
MRL/MpJ Tenocytes + MRL/MpJ-Derived Proteins
Full-Serum Media
24 Hours
Low-Serum/Secretome-Containing Media, Changed Every 2 Days
7 Days
0 Hour
Seed Cells onto Collagen/dPECM-Coated Substrates (Low Density)
1 Day
Secretome Treatment
8 Days
Fix, Stain, & Confocal Imaging
Cell & ECM Alignment, ECM Deposition
Gap Junctions (Cx-43)
Myofibroblast Activity (αSMA)
B
Baseline B6 vs. MRL/MpJ (Low-Serum)
F-actin Coherency
Fibronectin IntDen / Cell (Normalized to B6)
Collagen I IntDen / Cell (Normalized to B6)
Cx-43 IntDen / Cell (Normalized to B6)
P = 0.095
B6
MRL
C
F-actin & DAPI
Fibronectin
Connexin-43
Merged
B6/MRL dECM
B6/MRL Sec
BB
BM
MM
D
E
BB
BM
MM
dECM
Secretome
Both
Cx-43 IntDen / Cell (Normalized to Cells Alone)
F
Experimental Groups
Full-Serum Media
Low-Serum/Secretome-Containing Media, Changed Every 2 Days
3 Days
0 Hour
Seed Cells onto Uncoated/dPECM-Coated Substrates (High Density)
1 Day
Secretome Treatment
4 Days
Fix, β-Galactosidase Staining, & Imaging
Cell Senescence & Cell Counting
B6/MRL dECM
B6/MRL Sec
BB
BM
MM
G
% ß-Galactosidase+ Cells
P = 0.074
Total Cell Number

1437

1438 **Fig. 7. A recombinant protein therapeutic comprised of MRL/MpJ-enriched**
1439 **structural and soluble factors phenocopies MRL/MpJ cell behavior in**
1440 **Sprague-Dawley rat tenocytes *in vitro***. (**A**) Experimental design of recombinant
1441 protein therapeutic development and *in vitro* culture model for single-cell and
1442 confluent cell experiments. (**B**) Representative cell outlines of Sprague-Dawley
1443 (SD) rat tenocytes cultured with B6 or MRL/MpJ-derived components or the
1444 recombinant protein therapeutic (scale bar, 100 μm) to visualize cytoskeletal
1445 morphology and cellular protrusions. (**C and D**) SD tenocytes treated with
1446 MRL/MpJ-derived components and the recombinant protein therapeutic exhibited
1447 identical (or superior in the protein therapeutic) cellular protrusion characteristics
1448 (C) and single-cell morphology (D) that were significantly different from SD
1449 tenocytes treated with B6-derived components. (**E**) IF staining of F-actin (grey)
1450 and fibronectin (green) of confluent SD tenocytes treated with mouse-derived
1451 components or the recombinant protein therapeutic (scale bar, 100 μm). (**F**) SD
1452 tenocytes treated with the recombinant protein therapeutic showed significantly
1453 higher F-actin alignment and similar fibronectin deposition compared to SD
1454 tenocytes treated with mouse-derived components. Total cell number was
1455 significantly reduced by the recombinant protein therapeutic relative to the
1456 MRL/MpJ-derived components. $^{*}P < 0.05$, $^{**}P < 0.01$, $^{***}P < 0.001$, $^{****}P <$
1457 0.0001. Significance was determined using a one-way Welch's ANOVA with post-
1458 hoc Games-Howell for cell morphology, total protrusion length, and total cell
1459 number data. For cellular protrusion and fibronectin deposition data, significance
1460 was determined using a one-way ANOVA with post-hoc Tukey (percentage of
1461 cells with protrusions) or Kruskal-Wallis test with post-hoc Dunn's (number of
1462 protrusions, normalized total protrusion length, normalized fibronectin integrated
1463 density). Representative images shown for all staining experiments.
1464

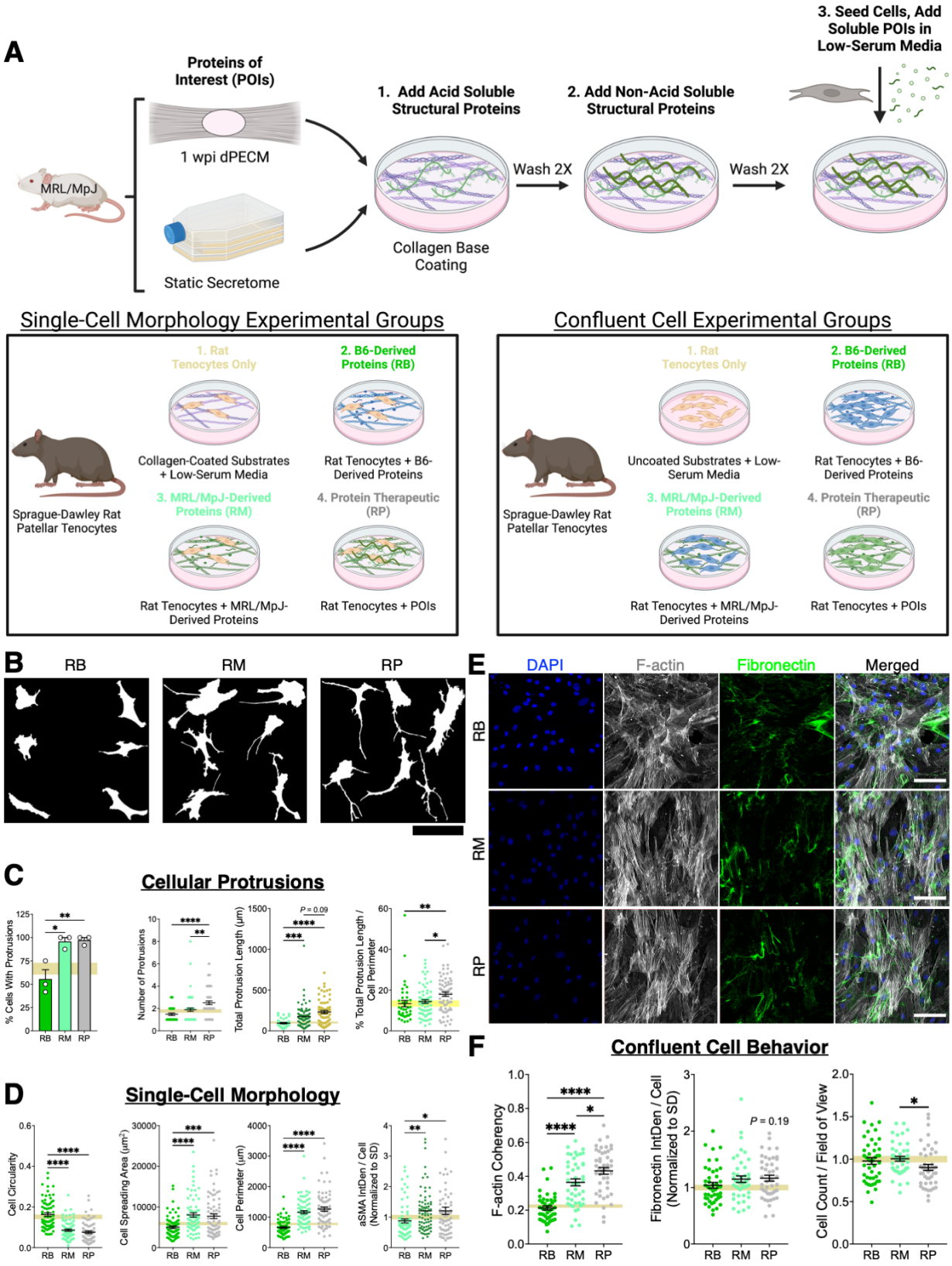
A
Proteins of Interest (POIs)
1 wpi dPECM
MRL/MpJ
Static Secretome
1. Add Acid Soluble Structural Proteins
Collagen Base Coating
Wash 2X
2. Add Non-Acid Soluble Structural Proteins
Wash 2X
3. Seed Cells, Add Soluble POIs in Low-Serum Media
Single-Cell Morphology Experimental Groups
1. Rat Tenocytes Only
Collagen-Coated Substrates + Low-Serum Media
2. B6-Derived Proteins (RB)
Rat Tenocytes + B6-Derived Proteins
3. MRL/MpJ-Derived Proteins (RM)
Rat Tenocytes + MRL/MpJ-Derived Proteins
4. Protein Therapeutic (RP)
Rat Tenocytes + POIs
Sprague-Dawley Rat Patellar Tenocytes
Confluent Cell Experimental Groups
1. Rat Tenocytes Only
Uncoated Substrates + Low-Serum Media
2. B6-Derived Proteins (RB)
Rat Tenocytes + B6-Derived Proteins
3. MRL/MpJ-Derived Proteins (RM)
Rat Tenocytes + MRL/MpJ-Derived Proteins
4. Protein Therapeutic (RP)
Rat Tenocytes + POIs
Sprague-Dawley Rat Patellar Tenocytes
B
RB
RM
RP
C
Cellular Protrusions
% Cells With Protrusions
Number of Protrusions
Total Protrusion Length (μm)
P = 0.09
% Total Protrusion Length / Cell Perimeter
D
Single-Cell Morphology
Cell Circularity
Cell Spreading Area (μm²)
Cell Perimeter (μm)
aSMA IntDen / Cell (Normalized to SD)
E
DAPI
F-actin
Fibronectin
Merged
F
Confluent Cell Behavior
F-actin Coherency
Fibronectin IntDen / Cell (Normalized to SD)
P = 0.19
Cell Count / Field of View

1472 **Table 1. Structural and soluble recombinant proteins enriched in the MRL/MpJ**
1473 **provisional extracellular matrix and secretome identified using quantitative**
1474 **proteomics**.

Role	Protein Name	Company	Product	Concentration (µg/mL)
Base	**Collagen, type I, alpha 1 (Col1a1)**	**Thermo Fisher Scientific**	**A1048301**	**500**
Structural Proteins (ECM Coating)	**Collagen, type VI, alpha 1 (Col6a1)**	**MyBioSource**	**MBS2105170**	**0.1**
	Collagen, type VI, alpha 3 (Col6a3)	**MyBioSource**	**MBS634441**	**0.1**
	Decorin	**R&D Systems**	**1060-DE**	**1**
	Fibrillin	**GeneTex**	**GTX00048-PRO**	**0.25**
	Fibrinogen	**LSBio**	**LS-G13486**	**100**
	Fibronectin	**Thermo Fisher Scientific**	**33-016-015**	**10**
	Inter-alpha-trypsin inhibitor heavy chain 1 (ITIH1)*	MyBioSource	MBS2009485	10
	Inter-alpha-trypsin inhibitor heavy chain 1 (ITIH3)*	Aviva Systems Biology	OPCA263725	10
	Periostin*			1
	Transforming growth factor βigh3 (TGFβigh3)	**R&D Systems**	**2559-BG**	**1**
Soluble Proteins (Exogenous Media Supplement)	Annexin A1 (ANXA1)*	Genetex	GTX00335	0.25
	Annexin A5 (ANXA5)*	LSBio	LS-G11883	0.25
	Annexin A6 (ANXA6)*	Sino Biological	11161-H08E	0.25
	CXCL1 (KC)	**R&D Systems**	**453-KC**	**0.01**
	CXCL5 (LIX)	**R&D Systems**	**433-MC**	**0.02**
	Epiregulin (EREG)	**Sino Biological**	**50559-M01H**	**0.0005**
	Fatty-acid-binding protein 4 (FABP4)	**R&D Systems**	**9840-CL**	**0.02**
	Follistatin (FST)	**Sino Biological**	**50035-M02S**	**0.1**
	Follistatin-like 1 (FSTL1)*	Sino Biological	51127-M02H	1
	Hepatocyte growth factor (HGF)	**Sino Biological**	**50038-MNAH**	**0.04**
	Interleukin 1 receptor antagonist (IL-1Ra)	MyBioSource	MBS2097334	
	Leptin	**R&D Systems**	**498-OB**	**0.001**

	Matrilin-2 (MATN2)	**R&D Systems**	**3234-MN**	**0.05**
	Matrix metalloproteinase-3 (MMP3)	**R&D Systems**	**548-MM**	**0.001**
	Protein disulfide-isomerase A3 (PDIA3)*	Novus Biologicals	NBP2-59883	3
	Prolyl isomerase (PPIase)*	Sino Biological	50296-M08E	0.5
	Peroxiredoxin 1 (PRDX1)*	MyBioSource	MBS206323	5
	S100-A11*	Sino Biological	50227-M07E	1
	Semaphorin 3F (SEMA3F)	**R&D Systems**	**3237-S3**	**0.05**

Bolded rows indicate the preliminary panel of 17 recombinant proteins that were evaluated in the present study.

*Indicates a protein that was unavailable at the time of experimentation and consequently was not evaluated in the present study.

1481 **Table 2. Top 30 activated and inhibited ingenuity pathway analysis upstream**
1482 **regulators from proteomic analyses of the static secretome**

Upstream Regulator	Molecule Type	Predicated Activation State	Activation Z-Score	*P* Value of Overlap
Activated in MRL/MpJ Secretome (Inhibited in B6 Secretome)				
ATP	chemical - endogenous mammalian	Activated	3.379	2.13E-11
FOS	transcription regulator	Activated	3.2	2.66E-21
ANGPT2	growth factor	Activated	3.086	1.04E-10
CG	complex	Activated	3.059	1.71E-17
cigarette smoke	chemical toxicant	Activated	3.034	2.35E-09
RORC	ligand-dependent nuclear receptor	Activated	2.8	4.95E-06
D-fructose	chemical - endogenous mammalian	Activated	2.791	2.21E-08
MTOR	kinase	Activated	2.758	8.07E-06
5-hydroxytryptamine	chemical - endogenous mammalian	Activated	2.722	3.73E-04
RAC1	enzyme	Activated	2.674	2.34E-09
TGFA	growth factor	Activated	2.622	3.20E-09
OLR1	transmembrane receptor	Activated	2.607	1.80E-08
S-nitroso-N-acetyl-DL-penicillamine	chemical reagent	Activated	2.596	2.91E-06
RIPK2	kinase	Activated	2.596	9.74E-08
JUN	transcription regulator	Activated	2.574	4.21E-25
ERK	group	Activated	2.56	3.21E-12
HRAS	enzyme	Activated	2.528	1.15E-15
IL10RA	transmembrane receptor	Activated	2.475	1.19E-19
dextran sulfate	chemical drug	Activated	2.448	1.14E-25
RETN	other	Activated	2.446	4.29E-09
F10	peptidase	Activated	2.429	2.84E-08
PTPN1	phosphatase	Activated	2.414	1.49E-05
UTP	chemical - endogenous mammalian	Activated	2.411	2.38E-06
EPHX2	enzyme	Activated	2.4	7.39E-08
collagenase	group	Activated	2.36	6.75E-10
Collagen type II	complex	Activated	2.357	1.35E-12

cisplatin	chemical drug	Activated	2.353	5.26E-12
5-O-mycolyl-beta-araf-(1->2)-5-O-mycolyl-alpha-araf-(1->1')-glycerol	chemical - endogenous non-mammalian	Activated	2.339	4.95E-06
NFKBIB	transcription regulator	Activated	2.306	1.93E-11
PTX3	other	Activated	2.304	1.31E-08
Inhibited in MRL/MpJ Secretome (Activated in B6 Secretome)				
DUSP1	phosphatase	Inhibited	-3.348	1.24E-13
vitamin E	chemical drug	Inhibited	-3.265	4.17E-09
beta-estradiol	chemical - endogenous mammalian	Inhibited	-3.128	4.84E-28
SB-431542	chemical reagent	Inhibited	-2.884	5.93E-11
UCP1	transporter	Inhibited	-2.813	3.28E-03
estrogen receptor	group	Inhibited	-2.782	1.51E-14
MEOX2	transcription regulator	Inhibited	-2.722	7.88E-12
ESR1	ligand-dependent nuclear receptor	Inhibited	-2.708	5.43E-13
NOTCH2	transcription regulator	Inhibited	-2.588	5.77E-06
genistein	chemical drug	Inhibited	-2.568	4.45E-16
STK11	kinase	Inhibited	-2.53	4.81E-10
INPP5D	phosphatase	Inhibited	-2.456	1.56E-06
pimagedine	chemical drug	Inhibited	-2.449	1.87E-06
MSC	transcription regulator	Inhibited	-2.449	2.00E-04
FBXO32	enzyme	Inhibited	-2.438	1.60E-03
diphenyleneiodonium	chemical reagent	Inhibited	-2.428	4.09E-08
actinomycin D	biologic drug	Inhibited	-2.421	3.18E-16
TAF4	transcription regulator	Inhibited	-2.412	1.78E-08
Traj18	other	Inhibited	-2.401	4.54E-09
CHRNA7	transmembrane receptor	Inhibited	-2.397	9.90E-06
tosylphenylalanyl chloromethyl ketone	chemical - protease inhibitor	Inhibited	-2.395	1.46E-06

SB203580	chemical drug	Inhibited	-2.388	6.20E-24
Y 27632	chemical drug	Inhibited	-2.384	9.29E-11
metformin	chemical drug	Inhibited	-2.375	3.08E-08
Hbb-b1	transporter	Inhibited	-2.359	1.04E-05
TET2	enzyme	Inhibited	-2.353	2.87E-04
tempol	chemical drug	Inhibited	-2.345	3.63E-09
Sb202190	chemical drug	Inhibited	-2.342	1.02E-07
APC	enzyme	Inhibited	-2.338	1.79E-14
caffeic acid phenethyl ester	chemical drug	Inhibited	-2.336	8.03E-10

1483

1484 **Table 3. Increased and decreased ingenuity pathway diseases and functions from**
1485 **proteomic analyses of the static secretome**
1486

Diseases or Function Annotation	Categories	Predicated Activation State	Activation Z-Score	*P* Value of Overlap
Increased in MRL/MpJ Secretome (Decreased in B6 Secretome) – 8 Total				
Mitogenesis	Cell Cycle	Increased	2.794	1.61E-31
Angiogenesis of lesion	Organismal Injury and Abnormalities	Increased	2.459	2.62E-21
Invasion of malignant tumor	Cancer, Organismal Injury and Abnormalities, Tumor Morphology	Increased	2.343	7.61E-23
Organismal death	Organismal Survival	Increased	2.286	4.16E-39
Morbidity or mortality	Organismal Survival	Increased	2.203	7.78E-42
Binding of breast cancer cell lines	Cell-To-Cell Signaling and Interaction	Increased	2.166	4.24E-26
Migration of vascular cells	Cellular Movement	Increased	2.028	3.10E-26
Invasion of tumor	Cancer, Organismal Injury and Abnormalities, Tumor Morphology	Increased	2.004	3.31E-25
Decreased in MRL/MpJ Secretome (Increased in B6 Secretome) – 11 Total				
Cytotoxicity of lymphatic system cells	Cell Death and Survival, Cellular Compromise	Decreased	-2.434	1.08E-29
Cytotoxicity of cells	Cell Death and Survival, Cellular Compromise	Decreased	-2.349	2.23E-26
Toxicity of cells	Cell Death and Survival, Cellular Compromise	Decreased	-2.315	3.81E-28
Cytotoxicity of lymphocytes	Cell Death and Survival, Cellular Compromise	Decreased	-2.313	1.03E-28
Expansion of T lymphocytes	Cellular Development, Cellular Growth and Proliferation, Hematological System Development and Function, Lymphoid Tissue Structure and Development	Decreased	-2.268	5.76E-27

Cytotoxicity	Cell Death and Survival	Decreased	-2.166	3.32E-29
Cell movement of T lymphocytes	Cell-mediated Immune Response, Cellular Movement, Hematological System Development and Function, Immune Cell Trafficking	Decreased	-2.135	1.80E-35
T cell migration	Cell-mediated Immune Response, Cellular Movement, Hematological System Development and Function, Immune Cell Trafficking	Decreased	-2.116	5.83E-35
Expansion of lymphatic system cells	Cellular Growth and Proliferation, Lymphoid Tissue Structure and Development	Decreased	-2.09	9.39E-34
MAPKKK cascade	Cell Signaling	Decreased	-2.075	5.82E-30
Cell movement of macrophages	Cellular Movement, Hematological System Development and Function, Immune Cell Trafficking, Inflammatory Response	Decreased	-2.03	2.35E-41

1487

1488